

## Global ocean circulation during 1992–1997, estimated from ocean observations and a general circulation model

D. Stammer,<sup>1</sup> C. Wunsch,<sup>2</sup> R. Giering,<sup>3</sup> C. Eckert,<sup>2</sup> P. Heimbach,<sup>2</sup> J. Marotzke,<sup>4</sup> A. Adcroft,<sup>2</sup> C. N. Hill,<sup>2</sup> and J. Marshall<sup>2</sup>

Received 28 March 2001; revised 17 September 2001; accepted 15 October 2001; published 5 September 2002.

[1] A three-dimensional oceanic state is estimated for the period 1992–1997 as it results from combining large-scale ocean data sets with a general circulation model. At the cost of increased computational load, the estimation (assimilation) method is chosen specifically so that the resulting state estimate is consistent with the model equations, having no artificial sources or sinks. To bring the model into close agreement with observations, its initial temperature and salinity conditions are permitted to change, as are the time-dependent surface fluxes of momentum, heat and freshwater. Resulting changes of these “control vectors” are largely consistent with accepted uncertainties in the hydrographic climatology and meteorological analyses. The assimilation procedure is able to correct for many of the traditional shortcomings of the flow field by changing the surface boundary conditions. Changes in the resulting flow field are predominantly on the gyre scale and affect many features that are often poorly simulated in traditional numerical simulations, such as the strengths of the Gulf Stream and its extension, the Azores Current and the anticyclonic circulation associated with the Labrador Sea. Tests of the results and their consistency with prior error assumptions show that the constrained model has moved considerably closer to the observations imposed as constraints, but has also moved closer to independent data from the World Ocean Circulation Experiment not used in the assimilation procedure. In some regions where the comparisons remain indeterminate, not enough ocean observations are available, and it is difficult to ascribe the residuals to either the model or the observations. Although problems remain, a useful first solution to the global time-dependent ocean state estimation problem has been found. The estimates will continue to improve through the evolution of numerical models, computer power increases, more data, and more efficient estimation methods. *INDEX TERMS:* 4532 Oceanography: Physical: General circulation; 4556 Oceanography: Physical: Sea level variations; 4504 Oceanography: Physical: Air/sea interactions (0312); 4255 Oceanography: General: Numerical modeling; *KEYWORDS:* state estimation, data assimilation, numerical modeling, data synthesis, ocean circulation

**Citation:** Stammer, D., C. Wunsch, R. Giering, C. Eckert, P. Heimbach, J. Marotzke, A. Adcroft, C. N. Hill, and J. Marshall, Global ocean circulation during 1992–1997, estimated from ocean observations and a general circulation model, *J. Geophys. Res.*, 107(C9), 3118, doi:10.1029/2001JC000888, 2002.

### 1. Introduction

[2] Because the ocean circulation shows vigorous variability on a wide range of temporal and spatial scales, a substantial emphasis has to be put on adequately observing it. Many of the most important scientific properties of the circulation, for example, its fluxes of heat, carbon, or

potential vorticity, are never actually measured, but can only be calculated from estimates of the circulation. A combination of regional or global ocean data sets with a state-of-the-art numerical circulation model is therefore required to exploit the diverse data types and to obtain the best estimate of the time-varying ocean circulation. This process, known as ocean state estimation, has some commonality with ongoing analysis and reanalysis activities in the atmospheric community. However, there are substantial differences from meteorological procedures, because the present focus is much less on forecasting and much more on estimating the oceanic state to improve our understanding of ocean dynamics. Furthermore, the technologies of oceanic observation are sometimes radically different from those used in the atmosphere, and this consideration also leads to differing estimation problems and solutions.

<sup>1</sup>Scripps Institution of Oceanography, La Jolla, California, USA.

<sup>2</sup>Earth and Planetary Science Department, Massachusetts Institute of Technology, Cambridge, Massachusetts, USA.

<sup>3</sup>FastOpt, Hamburg, Germany.

<sup>4</sup>Southampton Oceanography Centre, University of Southampton, Southampton, UK.

**Table 1.** Model Layer Thicknesses and Center Depths (in Meters)

Level	Thickness	Layer Center
1	10	5
2	10	15
3	15	27.5
4	20	45
5	20	65
6	25	87.5
7	35	117.5
8	50	160
9	75	222.5
10	100	310
11	150	435
12	200	610
13	275	847.5
14	350	1160
15	415	1542.5
16	450	1975
17	500	2450
18	500	2950
19	500	3450
20	500	3950
21	500	4450
22	500	4950

Finally, the much smaller dynamical scales present in the ocean present a greater computational burden.

[3] A complete ocean state estimation system will eventually combine the entire suite of large-scale ocean observations of all types, with the dynamics represented by an ocean circulation model. The aim of this paper is to introduce a prototype of such an estimation system, but one that uses a major subset of available ocean data, and a nearly complete model physics. Our primary focus here is on the time-evolving global circulation as it emerges from the monthly mean [Levitus *et al.*, 1994a, 1994b] hydrographic climatology, monthly mean [Reynolds and Smith, 1994] sea surface temperature (SST) fields, the altimetric measurements from TOPEX/Poseidon (T/P), ERS-1, and ERS-2, and daily surface forcing over the time interval 1992–1997. These prototype results are sufficiently conclusive to be scientifically useful, and they demonstrate that a complete World Ocean Circulation Experiment (WOCE) type data synthesis is now possible and that ongoing, near-operational ocean state estimates are at hand.

[4] Results will be presented in several papers. Here, in paper one we describe details of the model and the optimization, and provide an overall description of the estimated mean state and the seasonal variability in the solution. This includes a test of the results through comparison with independent information available from large-scale WOCE data sets, including the global hydrography, the expendable bathythermograph (XBT) data. A more thorough analysis of the estimated state for oceanic property transports and pathways is given by D. Stammer *et al.* (Volume, heat, and freshwater transports of the global ocean circulation 1992–1997, estimated from a general circulation model constrained by WOCE data, submitted to *Journal of Geophysical Research*, 2002) (hereinafter referred to as Stammer *et al.*, submitted manuscript, 2002a). Estimated surface fluxes are evaluated in detail by D. Stammer *et al.* (Estimates of surface momentum, heat and freshwater fluxes, obtained from combining an ocean circulation model with global ocean data sets, submitted to *Journal of Cli-*

*mate*, 2002) (hereinafter referred to as Stammer *et al.*, submitted manuscript, 2002b). Ponte *et al.* [2001] have already shown that the results have improved skill in predicting the Earth’s angular momentum balance in what is a globally integrated test of these results.

## 2. Formalism and Models

### 2.1. Formalism

[5] State estimation is a major part of control theory, in which one combines the dynamics embedded in models, statistical information in the form of a priori data and error covariances, and observations. Formally, we bring a numerical ocean model into consistency with observations by solving a constrained least squares optimization problem. Recent textbook accounts of ocean applications are provided by Bennett [1992] and Wunsch [1996], and there are numerous collections of research papers on this subject [e.g., Malanotte-Rizzoli, 1996]. We therefore summarize only briefly the present discrete-time methodology, using a notation adopted from Wunsch [1996].

[6] Algebraically, a general circulation model (GCM) can be written in canonical form as

$$\mathbf{x}(t+1) = \mathcal{L}[\mathbf{x}(t), \mathbf{B}\mathbf{q}(t), \mathbf{\Gamma}\mathbf{u}(t)] \quad (1)$$

where  $\mathbf{x}(t)$  is the state vector,  $\mathcal{L}$  represents the full nonlinear operator stepping the model forward in time starting from a prescribed initial condition  $\mathbf{x}(t_0)$ , and  $\mathbf{q}(t)$  represents all externally specified boundary conditions and also represents sources and sinks. The state vector contains all the physical variables (here, three components of velocity, pressure, temperature, and salinity) necessary to calculate the system one time step into the future, when given necessary boundary conditions. Matrices  $\mathbf{B}$  and  $\mathbf{\Gamma}$  are used to map the known surface forcing fields  $\mathbf{q}(t)$  and the unknown “controls”  $\mathbf{u}(t)$  onto the model grid. Formally, we think of  $\mathbf{u}(t)^T = [\mathbf{u}_0^T, \mathbf{u}_f^T, \boldsymbol{\epsilon}^T]$  as including separate components comprising errors in the initial conditions  $\mathbf{u}_0$ , the external forcing fields  $\mathbf{u}_f(t)$  and the internal model physics  $\boldsymbol{\epsilon}(t)$ . In the present experiment we keep  $\boldsymbol{\epsilon}(t) = 0$ ; but this restriction will be relaxed explicitly in future applications, for example, by making the viscosity and diffusivity coefficients control parameters.

[7] Most oceanographic measurements are approximately a linear combination of the model state vector, for example, velocity, temperature, and salinity, but are contaminated by noise,

$$\mathbf{y}(t) = \mathbf{E}(t)\mathbf{x}(t) + \mathbf{n}(t). \quad (2)$$

[8] The “observation matrix”  $\mathbf{E}$  relates the model state vector to observables and is normally very sparse, because observations usually involve only local subsets of  $\mathbf{x}(t)$ . Examples include along-track altimetric observations of the dynamically induced surface elevation, moored velocities time series at one point, or tomographic ray paths.

[9] In general terms, we seek an estimate,  $\tilde{\mathbf{x}}(t)$ , of the state vector and its uncertainty,  $\mathbf{P}(t)$ , that is consistent with the observations  $\mathbf{y}(t)$  and their uncertainties  $\mathbf{R}(t)$  and with the model dynamics (equation (1)) and its uncertainty  $\mathbf{Q}(t)$ . Reflecting the structure of  $\mathbf{u}$ ,  $\mathbf{Q}$  contains contributions from the initial conditions, the internal model physics, and the external forcing, i.e.,  $\mathbf{Q}^T = [\mathbf{Q}_0^T, \mathbf{Q}_f^T, \mathbf{Q}_\epsilon^T]$ . The control

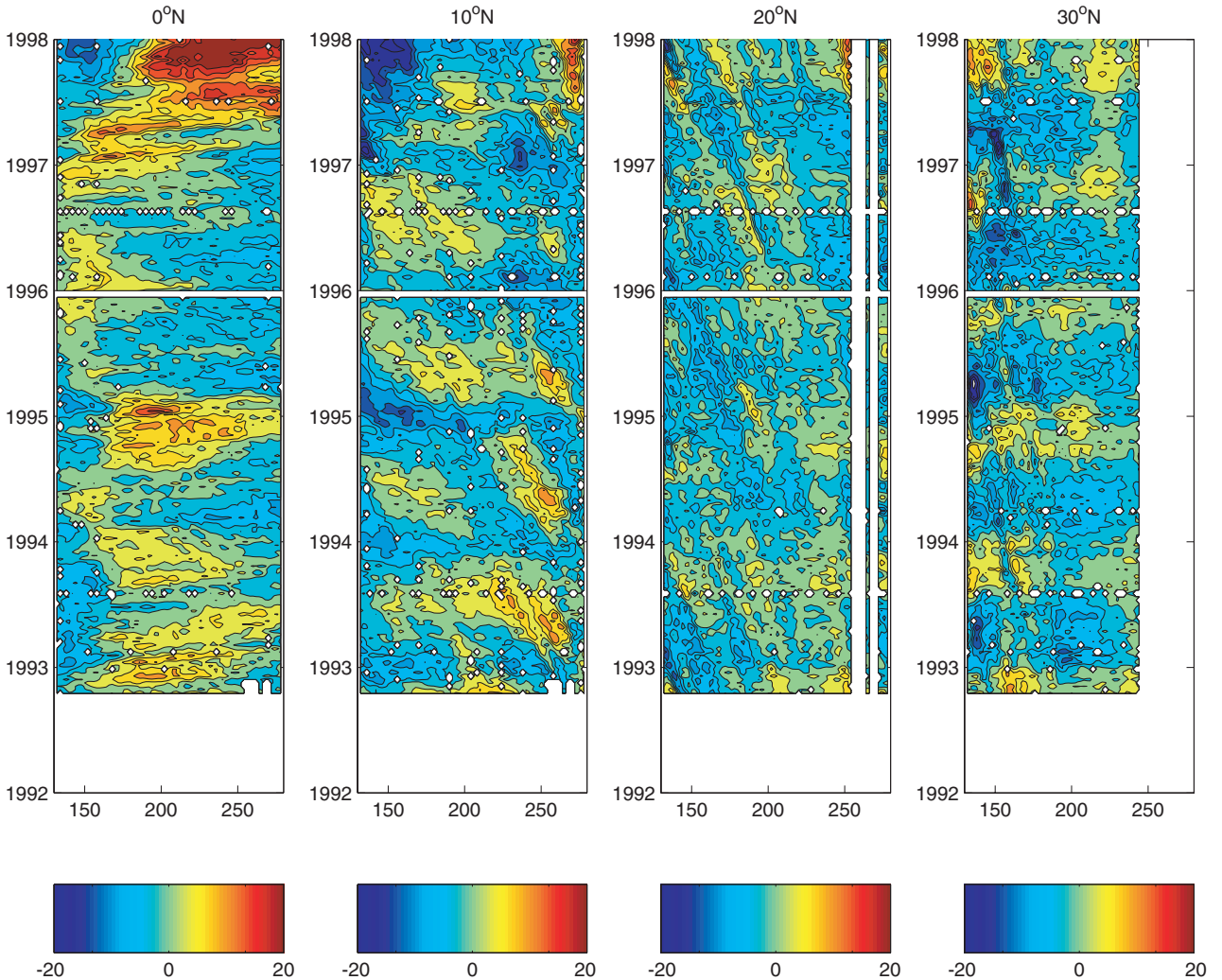


**Figure 1.** Longitude-time sections for TOPEX/Poseidon sea surface height (SSH) anomalies for, from left to right,  $0^{\circ}\text{N}$ ,  $10^{\circ}\text{N}$ ,  $20^{\circ}\text{N}$ , and  $30^{\circ}\text{N}$ . Contour interval is 5 cm. White regions mark data gaps and continents.

variables are modified from their initial values so as to produce the change in the estimated  $\mathbf{x}(t)$  that minimizes the model-data misfit measured by the quadratic “objective” or “cost” function,

$$J = \sum_{t=1}^{t_f} (\mathbf{y}(t) - \mathbf{E}\tilde{\mathbf{x}}(t))^T \mathbf{W}(t) (\mathbf{y}(t) - \mathbf{E}\tilde{\mathbf{x}}(t)) \quad (3)$$

subject to the model physics constraints. The model is enforced by appending it to the cost function in the form

$$L = J + \mathbf{u}_0^T \mathbf{Q}_0^{-1} \mathbf{u}_0 + \sum_{t=0}^{t_f-1} \left[ \boldsymbol{\epsilon}^T(t) \mathbf{Q}_e^{-1}(t) \boldsymbol{\epsilon}(t) + \mathbf{u}_f^T(t) \mathbf{Q}_f(t)^{-1} \mathbf{u}_f(t) \right] - 2 \sum_{t=0}^{t_f-1} \boldsymbol{\mu}(t+1)^T \{ \mathbf{x}(t+1) - \mathcal{L}[\mathbf{x}(t), \mathbf{B}\mathbf{q}(t), \boldsymbol{\Gamma}\mathbf{u}(t)] \}, \quad (4)$$

with the  $\boldsymbol{\mu}(t)$  being Lagrange multipliers and  $t_f$  being the final time step. By setting the derivatives of  $L$  with respect to  $\mathbf{u}$ ,  $\boldsymbol{\mu}$ , and  $\mathbf{x}$  to zero, we find that the conditions for a stationary value of  $L$  (a constrained minimum of  $J$ ) must satisfy the “normal equations” [see Wunsch, 1996]. Here,

these equations are not explicitly formed; rather, the stationary value of equation (5) is found by an iterative process over the entire space and time domain.

[10] A number of examples exist in the literature of simplified state estimation methods based upon, for example, nudging or variations of objective mapping [e.g., Masina *et al.*, 2001]. The method employed here was deliberately chosen to be potentially fully rigorous, so that at any given timestep, the solution would satisfy known equations of motion, and the time evolution between time steps would not involve any nonphysical sources or sinks, for example, of heat or momentum. The price paid is a substantially greater computational load; the gain is a dynamically consistent solution that can be given direct physical interpretation in terms of model physics and that is being exploited in subsequent papers (e.g., Stammer *et al.*, submitted manuscript, 2002a).

## 2.2. Models

[11] For the dynamics, we use the ocean general circulation model and its adjoint that have been developed at the

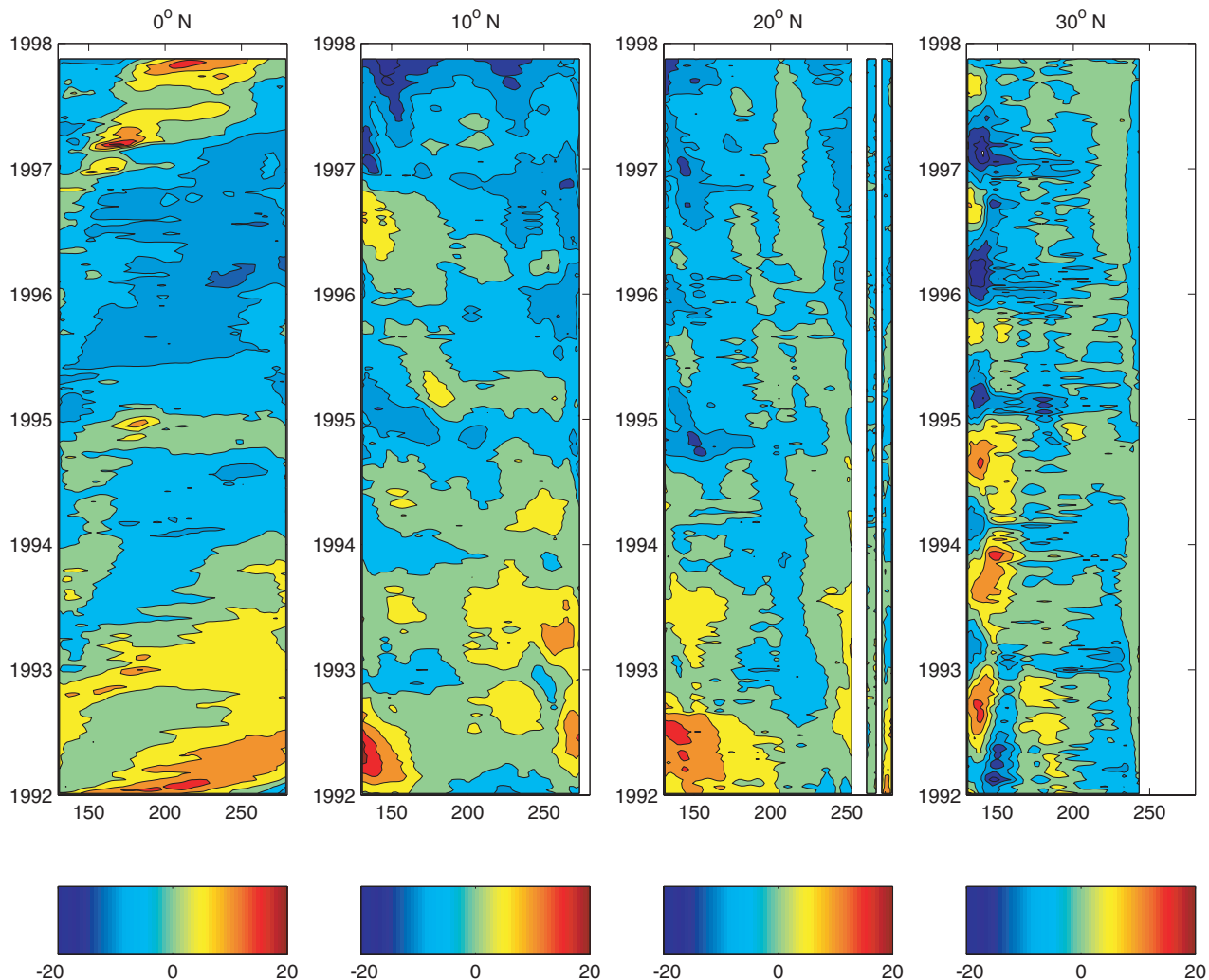


**Figure 2.** Longitude-time sections for SSH anomalies in unconstrained model for, from left to right,  $0^{\circ}\text{N}$ ,  $10^{\circ}\text{N}$ ,  $20^{\circ}\text{N}$ , and  $30^{\circ}\text{N}$ . Contour interval is 5 cm.

Massachusetts Institute of Technology (MIT-GCM). This model is based on the primitive equations on a sphere under the Boussinesq approximation. It consists of prognostic equations for horizontal velocity, heat, and salt and an equation of state that are integrated forward in time on a staggered “C” grid [Arakawa and Lamb, 1977]. At each time step the internal pressure is calculated from the hydrostatic relation, and the vertical velocity is diagnosed from continuity. Spatial coordinates are longitude, latitude, and height. A detailed description of the model is provided by Marshall *et al.* [1997a, 1997b]. For present purposes, we use a hydrostatic version with an implicit free surface. A full surface mixed layer model is used (called “KPP” [Large *et al.*, 1994]), and convective adjustment is used to remove gravitational instabilities underneath the surface mixed layer.

[12] The forward model is used to compute the model-data misfit. Without any adjustment to control variables, the initial “best guess” model-data misfit  $\mathbf{y}(t) - \mathbf{E}(t)\mathbf{x}(t)$  can be large. The adjoint model is used to provide the gradient of  $J$  with respect to the model variables; this

gradient is then used to modify the control variables so as to reduce the value of  $J$  in an iterative scheme. A standard optimizing descent algorithm (here a quasi-Newtonian method [see Gilbert and Lemaréchal, 1989]) is used with the gradient to determine the correction to the control terms.

[13] Coding the adjoint of a complex numerical model is time consuming and difficult, comparable in effort to development of the forward code itself. Some care was therefore taken in writing the MIT model, making it possible to obtain the adjoint code from the forward code in a semiautomatic way through automatic differentiation [Giering and Kaminski, 1998]. Marotzke *et al.*, [1999] give a full account of the construction of the adjoint model from the forward MIT-GCM code.

[14] In practice, this system of automatic adjoint code generation has proven to be extremely flexible, and it permits relatively easy regeneration of the adjoint code whenever a change in the forward model or objective function is necessary. We use the adjoint model here as a numerical means of finding a minimum of a constrained

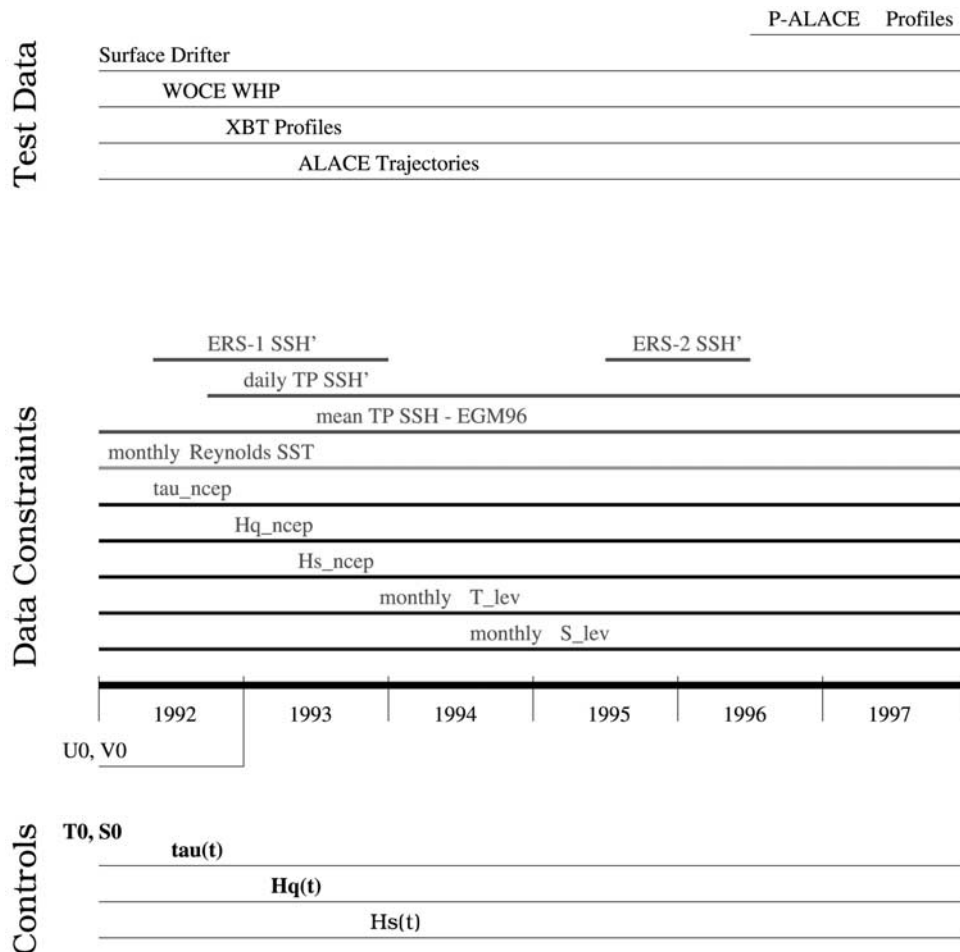


**Figure 3.** Schematic of the optimization. (top) Summary of withheld data sets used to test present solution. (middle) Data constraints imposed on model. (bottom) Summary of the control variables that are modified to produce optimal solution (horizontal velocity fields ( $u$ ,  $v$ ) are not part of control vector, but are adjusted geostrophically at the beginning to the new density field).

optimization problem. However, the associated adjoint solution itself has the important property of providing a measure of sensitivity of the cost function to the physical variables of the system; see *Marotzke et al.* [1999] for details.

[15] The GCM is configured globally with  $2^\circ$  horizontal resolution over  $\pm 80^\circ$  in latitude, with 22 levels in the vertical (see Table 1). Free-slip bottom and nonslip lateral wall boundary conditions are used. Laplacian viscosity and diffusivities are used, with  $\nu_h = 5 \times 10^4$  and  $\kappa_h = 10^3$  and with  $\nu_v = 10^{-3}$  and  $\kappa_v = 10^{-5}$  in the horizontal and vertical, respectively. Near the sea surface the vertical coefficients are specified by the KPP mixed layer model and can therefore be higher by an order of magnitude or more than given above in the surface mixed layer. To allow a time step of 1 hour, an implicit scheme was implemented for the vertical mixing.

[16] Approximate initial conditions were obtained from the *Levitus et al.* [1994a, 1994b] January potential temperature and salinity fields, with the velocity field then adjusted over a 1-month period. Daily values of surface heat and freshwater fluxes, and twice-daily values of windstress, all obtained from the National Center for Environmental Pre-

diction (NCEP)/National Center for Atmospheric Research (NCAR) reanalysis project, are used.

### 2.3. Testing the Forward Model

[17] Before attempting to combine a model with observations, one must compare the model to the observations to assure that they are consistent within the estimated uncertainties of both. Prior to the present work, the GCM was tested in a variety of configurations summarized by *Marshall et al.* [1997b], *Ponte et al.* [1998], and *Ponte and Stammer* [1999]. Here we have simulated, as a control run, the ocean circulation from 1992 through 1997. In the estimation procedure that follows later, a pure surface flux boundary condition is used; it leads to adjusted surface flux fields that are consistent with the ocean data. In the control run, however, simple use of the NCEP flux fields without the adjustments leads to extremely poor model results. For this reason, in the reference solution, the model  $\theta$ ,  $S$  fields in the surface layer are also relaxed toward climatological monthly mean fields with a 30-day time-scale.

[18] As a representative example of the many control model results, observations of the sea surface height (SSH)

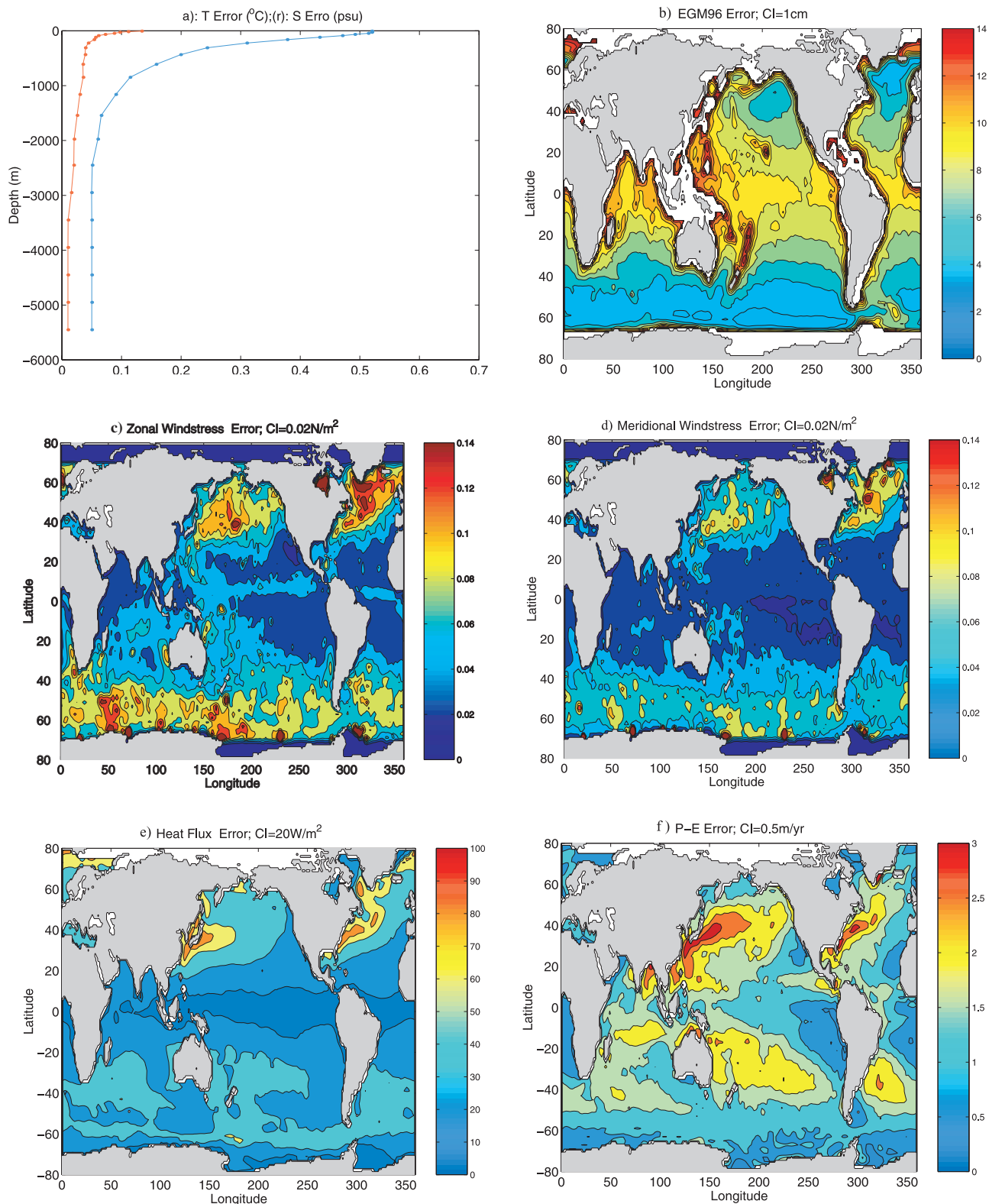


**Figure 4.** (a) Uncertainty profiles prescribed for potential temperature (blue) and salt (red) as a function of depth. (b) Diagonal elements of EGM96 error covariance matrix (cm). Root-mean-square (RMS) uncertainties for (c) zonal and (d) meridional wind stress components. Fields were obtained as RMS differences between NSCAT scatterometer wind stress measurements and simultaneous European Centre for Medium-Range Weather Forecasts (ECMWF) wind stress analyses (D. Chelton, personal communication, 1998). RMS uncertainties for (e) heat and (f) freshwater fluxes estimated from 30% and 100% of local RMS variabilities of National Centers for Environmental Prediction (NCEP) forcing fields.

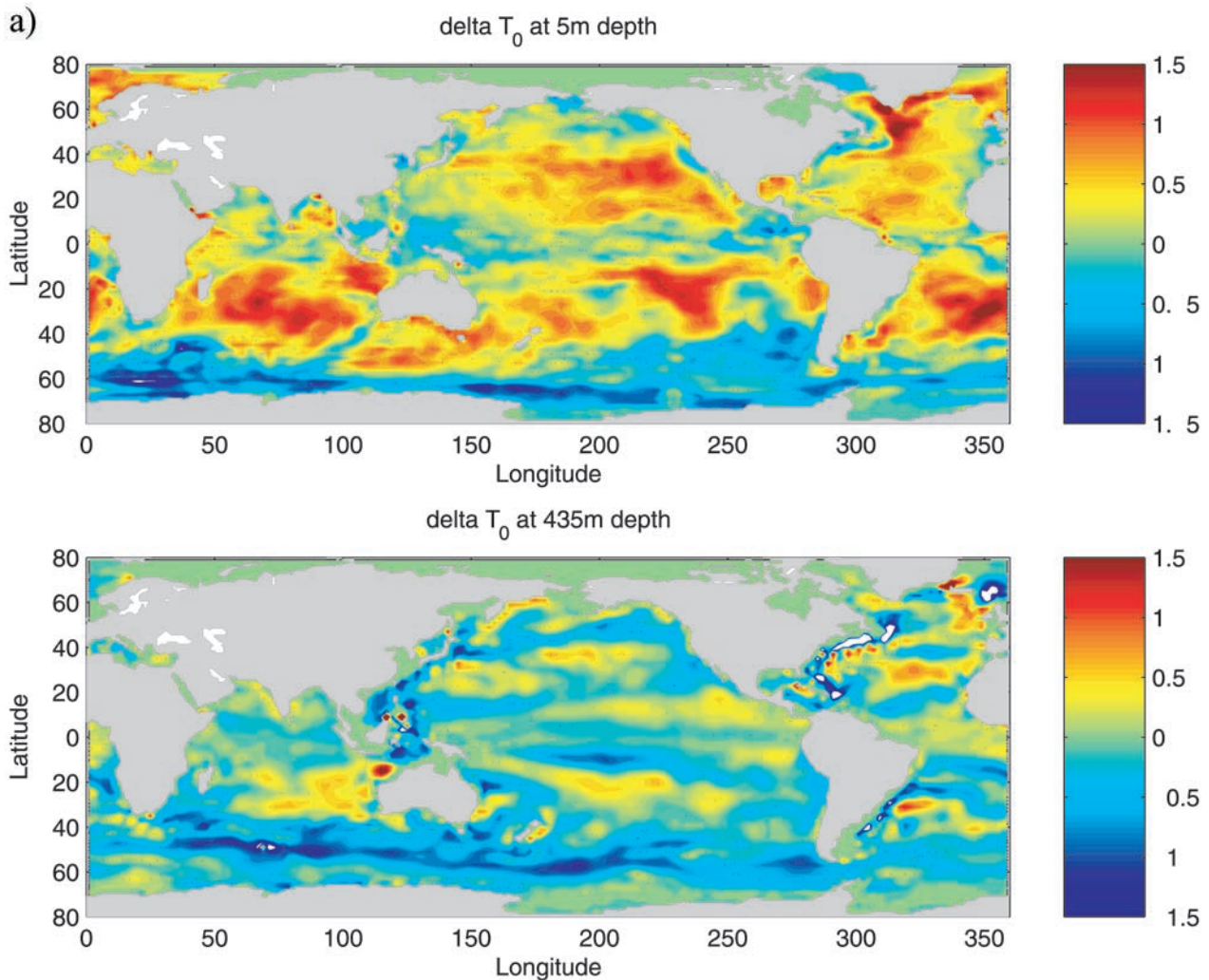


**Figure 5.** Adjustments of initial *Levitus et al.* [1994a, 1994b] January mean (a)  $\theta$  and (b)  $S$  fields at 5 and 435 m depth, respectively.

anomalies as observed by T/P are shown in Figure 1 along various time-longitude sections across the North Pacific Ocean. Qualitatively (Figure 2), the model compares reasonably well with the T/P observations: Spatial anomaly scales and amplitudes are similar, and several wave-like anomalies are successfully simulated, especially along the equator and associated with El Niño. Quantitatively, there exist differences, especially in middle and high latitudes, where the model fails to adequately simulate the observed seasonal SSH cycle. In addition, a clear model drift is obvious owing to inconsistent initial temperature and salinity conditions and surface flux fields. A goal of state estimation is to correct these deficiencies so that the resulting state lies within the ocean data uncertainties and the estimated control bounds.

### 3. Optimization

[19] The solution described below required  $\sim 100$  iterations, as described in section 2.3, to become acceptable. “Acceptable” means that the total value of  $J$  was consistent with the normalized average term having magnitude unity

and that to a first approximation, the distribution of individual terms approaches a  $\chi^2$  distribution. The latter requirement is only partially met, which we interpret as meaning that our initial estimates of observational and model noise are only approximations of the truth.

[20] A plausible first estimate for the control values would be zero, but the poor behavior of the control run in these circumstances suggested that a simple nonzero value could do significantly better. A traditional relaxation term was thus diagnosed, one that would keep the model temperature and salinity history on track with Levitus monthly mean fields. The time mean of the local relaxation term was used as the initial guess of the required changes to surface heat and salt fluxes. This step decreases the initial misfit substantially and thus reduces the number of required iterations [see also *Sirkes et al.*, 1996].

#### 3.1. Data Constraints

[21] In setting up  $J$ , mean and time-dependent components of surface elevation were separated, thus isolating errors owing to the geoid from the distinctly different ones in the time-evolving components. Surface forcing fields (wind

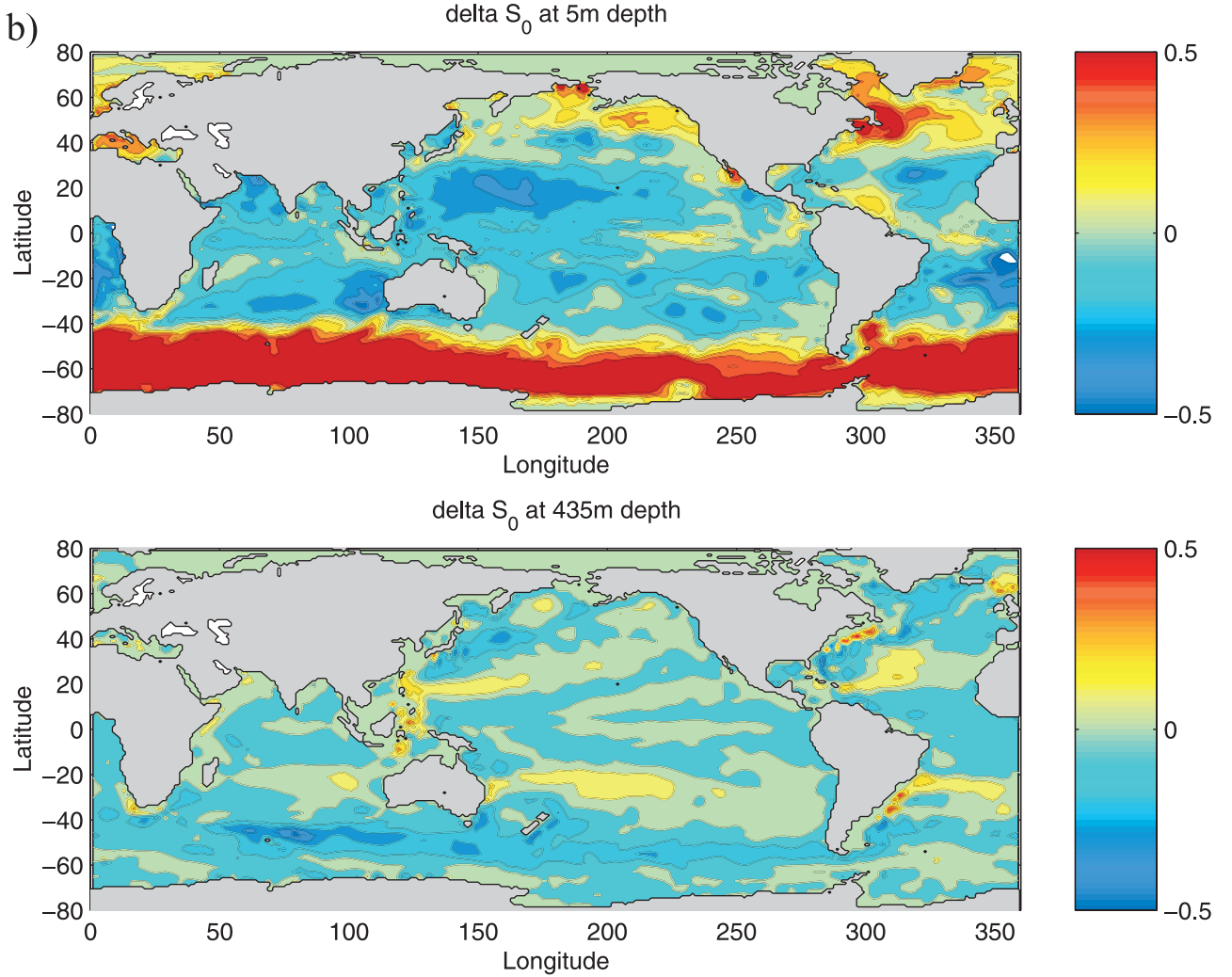


Figure 5. (continued)

stress, heat, and fresh water fluxes) and the initial hydrography were required to stay acceptably close to their starting values. In addition, monthly mean  $\theta$  and  $S$  fields were constrained every month by the monthly mean *Levitus et al.* [1994a, 1994b] climatology. The explicit form of  $J$  is then

$$\begin{aligned}
 J = & \frac{1}{2} \left[ \left( \bar{\eta} - \bar{\eta}_{tp} \right)^T \mathbf{W}_{\text{geoid}} \left( \bar{\eta} - \bar{\eta}_{tp} \right) \right. \\
 & + \left( \eta' - \eta'_{tp} \right)^T \mathbf{W}_{\eta_{tp}} \left( \eta' - \eta'_{tp} \right) + \left( \eta' - \eta'_{ers} \right)^T \mathbf{W}_{\eta_{ers}} \left( \eta' - \eta'_{ers} \right) \\
 & + \left( \delta \tau_x \right)^T \mathbf{W}_{\tau_x} \left( \delta \tau_x \right) + \left( \delta \tau_y \right)^T \mathbf{W}_{\tau_y} \left( \delta \tau_y \right) \\
 & + \left( \delta \mathbf{H}_Q \right)^T \mathbf{W}_{H_Q} \left( \delta \mathbf{H}_Q \right) + \left( \delta \mathbf{H}_F \right)^T \mathbf{W}_{H_F} \left( \delta \mathbf{H}_F \right) \\
 & + \left( \delta \mathbf{T}_0 \right)^T \mathbf{W}_T \left( \delta \mathbf{T}_0 \right) + \left( \delta \mathbf{S}_0 \right)^T \mathbf{W}_S \left( \delta \mathbf{S}_0 \right) \\
 & + \sum_i \left( \bar{\theta}_i - \bar{\theta}_{\text{SST}} \right)^T \mathbf{W}_{\text{SST}} \left( \bar{\theta}_i - \bar{\theta}_{\text{SST}} \right) \\
 & + \sum_i \left( \bar{\theta}_i - \bar{\theta}_{\text{Levi}} \right)^T \mathbf{W}_T \left( \bar{\theta}_i - \bar{\theta}_{\text{Levi}} \right) \\
 & + \sum_i \left( \bar{S}_i - \bar{S}_{\text{Levi}} \right)^T \mathbf{W}_S \left( \bar{S}_i - \bar{S}_{\text{Levi}} \right) \left. \right]. \quad (5)
 \end{aligned}$$

Here  $\bar{\theta}$ ,  $\bar{S}$ , indicate monthly mean potential temperature and salinity fields,  $\delta T$  and  $\delta S$  indicate changes in initial

conditions, and  $\delta H$  terms represent corrections to daily averages of surface momentum, heat, and freshwater flux fields. T/P and ERS altimeter anomalies are evaluated on a daily basis with along-track data averaged over  $2^\circ$  grid cells, and the mean T/P SSH field minus the EGM96 geoid model [Lemoine et al., 1997] is imposed over the entire period. The terms containing monthly mean *Levitus et al.* [1994a, 1994b] climatological fields are important ingredients and are required to adjust surface forcing fields that preserve the climatological water mass structures. The number of elements in each term is as follows: 5041; 2,601,148 (1,839,957 for T/P; 761,191 for ERS-1/2); 20,371,380; 20,371,380; 20,371,380; 169,778; 169,778; 669,744; 3,056,004; and 3,056,004 for a total of 91,213,017 elements. Note that the hydrography terms were down-weighted by a factor of 4, assuming that not every layer is statistically independent, and equivalent to the assumption that only about five vertical modes are necessary.

[22] From the above numbers it appears that we are trying to solve a somewhat underdetermined problem. However, a much more thorough analysis is required to determine the actual degrees of freedom in the data and control spaces, which fundamentally depends on spatial and temporal correlations, as well as on physical connections, for exam-



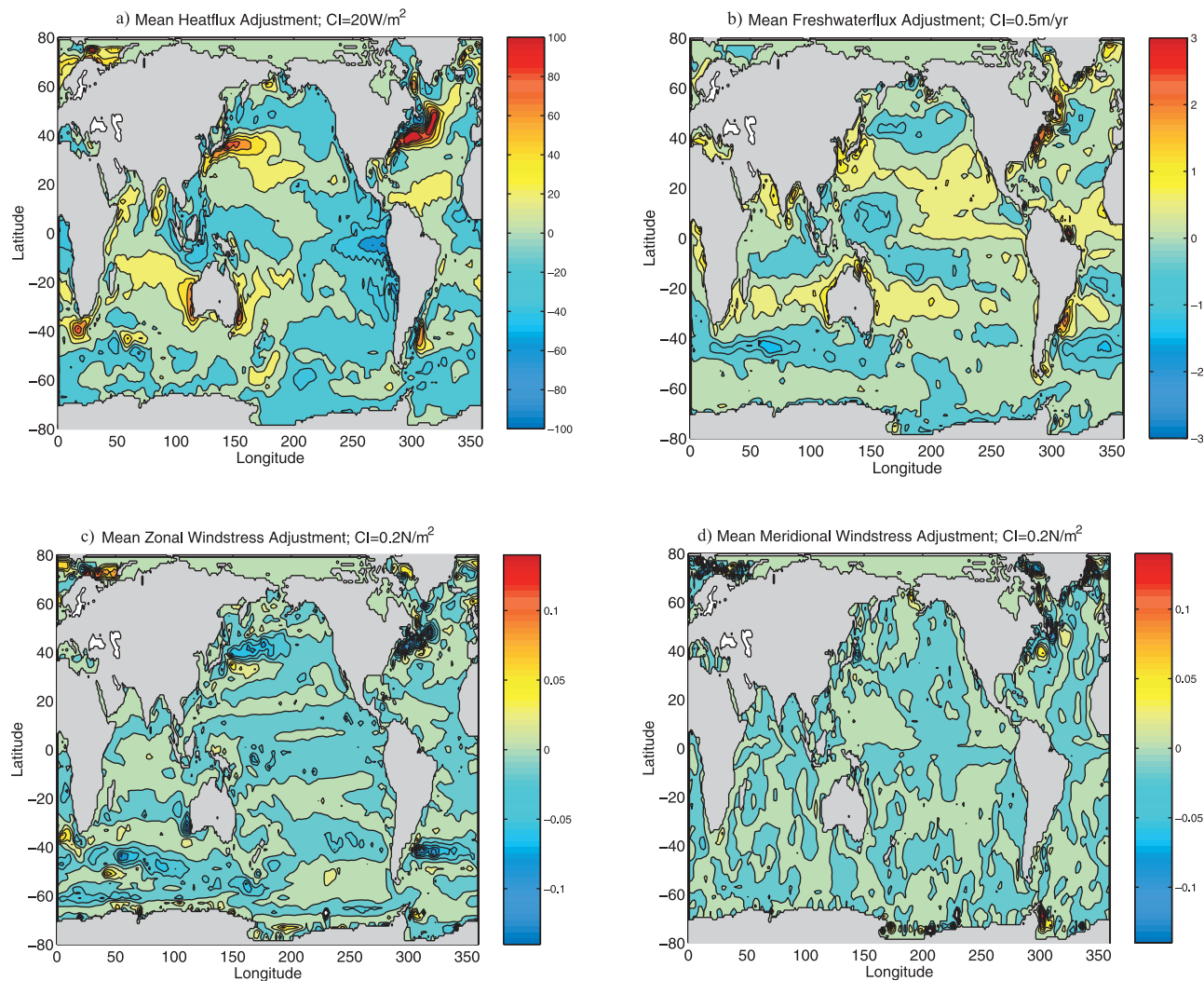


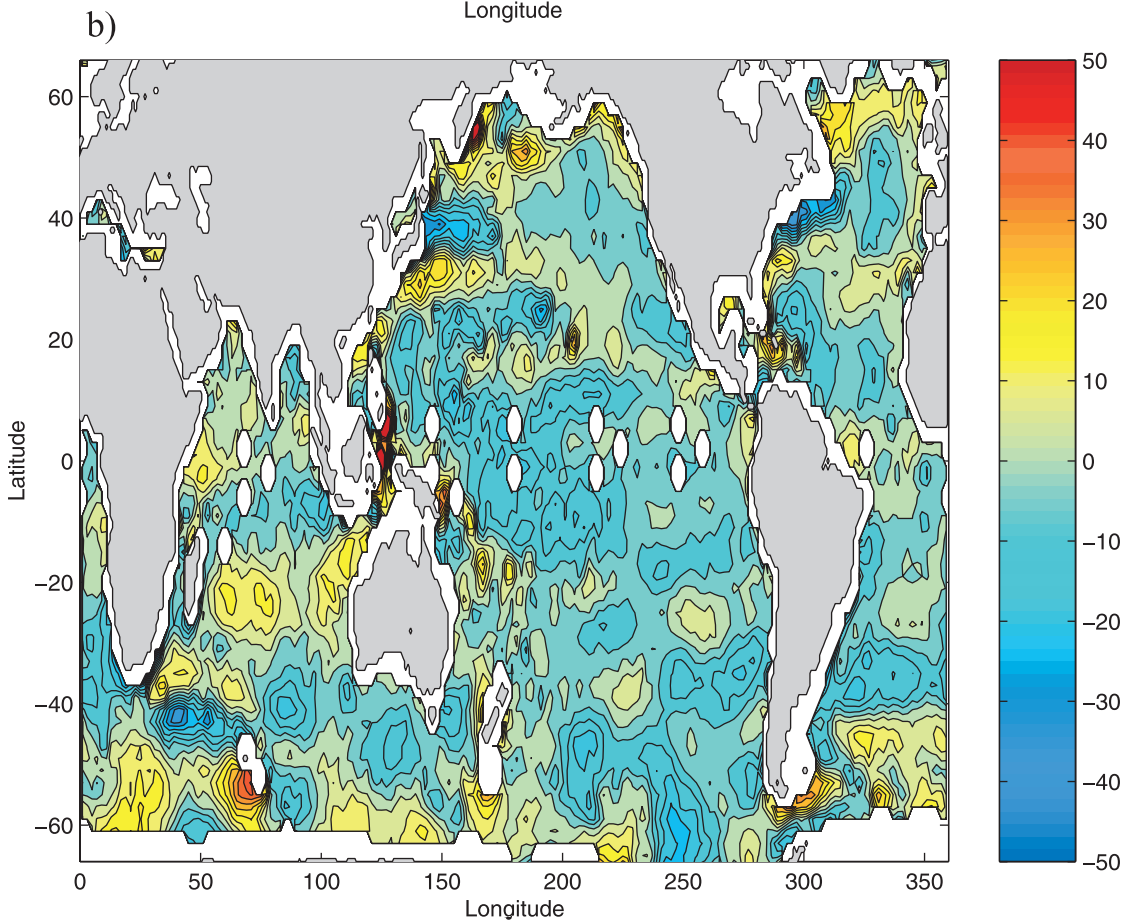
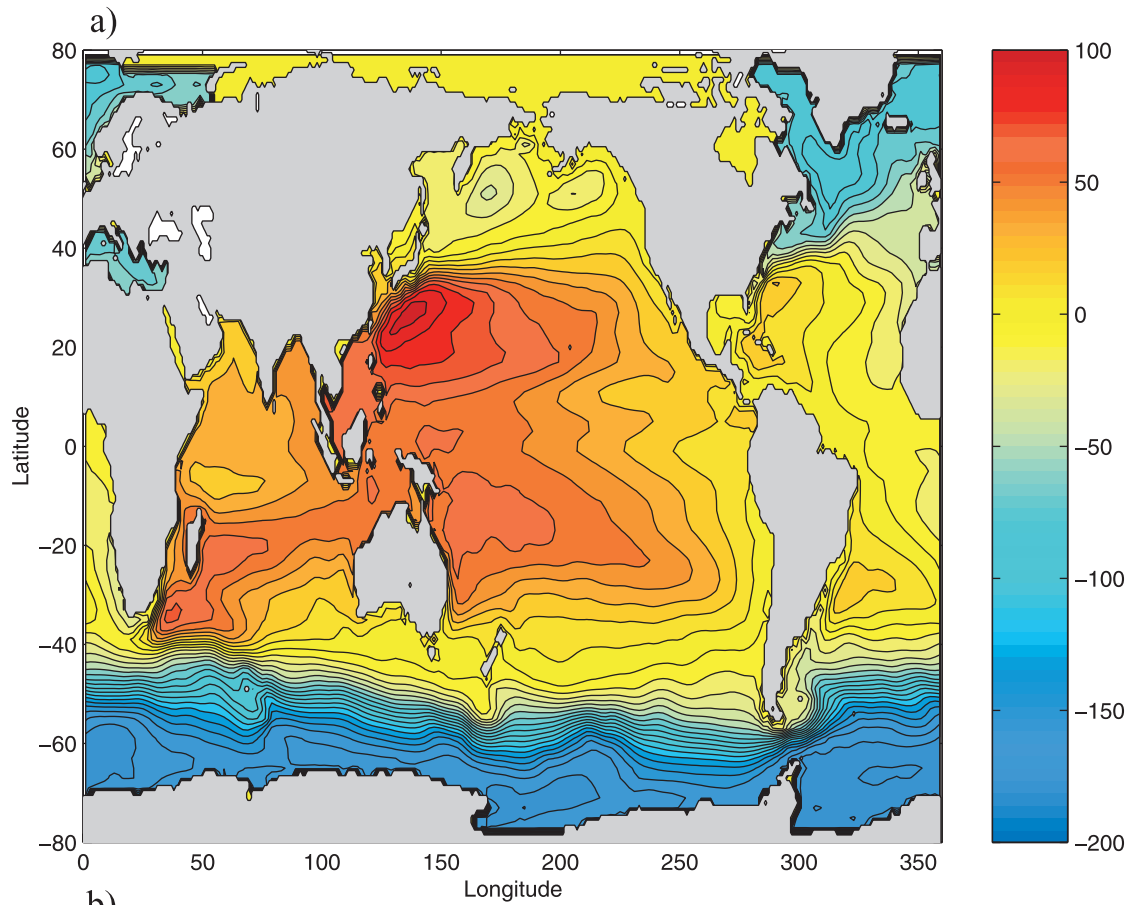
**Figure 6.** Mean changes of (a) net surface heat ( $\text{W m}^{-2}$ ) and (b) freshwater flux fields ( $\text{m yr}^{-1}$ ) as they result from optimization relative to prior NCEP fields. Net heat and freshwater flux fields are positive into the ocean. Mean (c) zonal and (d) meridional change of surface wind stress components as they result from optimization relative to NCEP first-guess fields ( $\text{N m}^{-2}$ , positive eastward and northward).

ple, between temperature and salinity through a T-S relation. But all of these dependencies are currently not built into the cost function. Formally underdetermined estimation problems are very common and familiar. They can be “regularized” in a number of ways. Here we impose a priori variances and covariances on the formal unknowns, including the noise. As textbooks describe [e.g., Wunsch, 1996], the covariances are equivalent to the imposition of just enough extra constraints to prevent ill conditioning. These constraints are tested as part of the assimilation procedure by comparing posterior statistics with the prior covariances. Note also that every observation constraint contains a noise or residual element, which is necessarily calculated as part of the solution. This renders [e.g., Wunsch, 1996, p.127] all estimation problems underdetermined and easily misunderstood.

[23] A schematic of the optimization setup is given in Figure 3. In the present calculation the control parameters include adjustments to the initial condition potential temperature ( $\theta$ ) and salinity ( $S$ ) fields, as well as to the daily

surface forcing fields over the full 6 years (see Figure 3, bottom); that is, we assume that the model uncertainties reside entirely in the initial conditions and surface forcing fields. Over the 6-year assimilation period the control vector has 130,753,664 elements.

[24] There is no guarantee that a descent procedure has found the “global minimum” as opposed to local or other equal minima. However, our first, and most important, goal is to produce an acceptable solution. To the extent that there might exist other equally valid fits of the model to the data, they must differ from the present solution by changes in one or more elements of the state or control vectors that the present observations cannot distinguish within uncertainty estimates. That is, unobserved elements of the general circulation could, in principle, be radically different in some other solution; for example, it is conceivable that there are large-scale recirculations at depth producing no surface signature detectable by the altimeter and yet remaining consistent with the climatologies. Whether such flows actually exist, and whether they are of any kinematical or



dynamical importance, remains to be determined. Comparisons presented in section 3.2 show that the estimated solution is, in general, much closer to the withheld ocean observations than is the first-guess solution.

### 3.2. Error Covariances

[25] The weight matrices  $\mathbf{W}$  in each term of  $J$  determine the solution to the minimization problem. In principle, one should specify the inverse of the full a priori error covariance matrix for each data type. In practice, however, this information is unavailable, and various ad hoc estimates must be used. For example, the mean hydrography terms were weighted using uncertainties ranging in the vertical from  $0.5^\circ\text{C}$  near the surface to  $0.05^\circ\text{C}$  at depth for potential temperature and ranging from 0.13 to 0.01 in salinity (Figure 4, reflecting the global uncertainties stated by *Levitus et al.* [1994a, 1994b]; no covariances were provided by them.

[26] The only nondiagonal inverse error covariance matrix used in the present calculation is  $\mathbf{W}_{\text{geoid}}$ , as provided with the EGM96 geoid model [*Lemoine et al.*, 1997]. However, because of the large size of  $\mathbf{W}_{\text{geoid}}$  when specified in geographical coordinates (it would have  $14,400^2 = 207,360,000$  elements), this term of the cost function is evaluated in spherical harmonic space up to degree and order 70 (producing the much smaller number  $71^2 \times 71^2 = 25,411,681$  for the number of terms). In Figure 4b the square root of the diagonal of the geoid error covariance is displayed over the ocean. Amplitudes range from  $\sim 15$  cm close to the equator to  $< 5$  cm in high latitudes. Enhanced errors can be found along major topographic structures such as ocean trenches or ridges. An additional error exists from the terms omitted from the geoid height estimate (spherical harmonic degree  $> 70$ ); like other such errors in the present system, these are described in the present computation as unstructured model error.

[27] If a model cannot reproduce some physics present in observations, one can regard the discrepancy as either a model error, described in the model error covariance  $\mathbf{Q}$ , or as a noise in the data, represented by data error covariance  $\mathbf{R}$ . For example, internal waves present in hydrography that a GCM does not resolve can be deemed as either a data noise or a model deficiency. The structure of explicit solutions to the state estimation problem [e.g., *Wunsch*, 1996] shows that the final state estimate is the same, no matter which view is taken. In the present case, for example, T/P data are specified as “along-track”  $2^\circ$  averages without any extra smoothing. The observed eddy variability in this data is treated as observational error, as the model does not resolve these features, and the SSH variance was down-weighted, therefore, by a factor of  $(1/2)^2$  of its total variance [cf. *Wunsch and Stammer*, 1998, Figure 8a].

[28] Wind stress components are downweighted by  $(\text{RMS difference})^{-2}$  between NASA scatterometer (NSCAT) observations and European Centre for Medium-Range Weather Forecasts (ECMWF) fields (Figures 4c and 4d) (D. Chelton, personal communication, 1998). NSCAT did not produce data from a full seasonal cycle, but the fields shown in

Figures 4c and 4d are the best available error estimates. For surface heat and fresh water fluxes, in the absence of any other information, a downweighting of  $(1/3)^2$  of their reciprocal local variances over the 6-year period was used (Figures 4e and 4f).

## 4. Estimated Ocean State

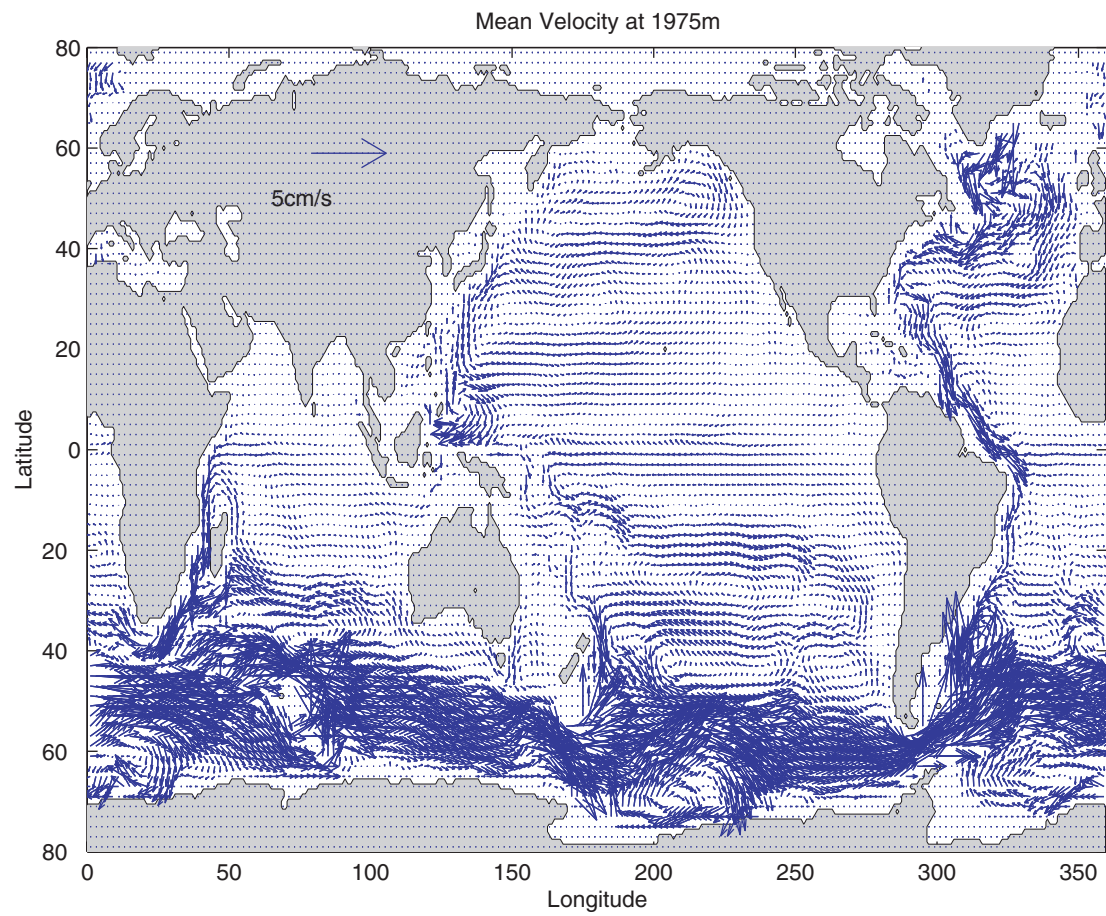
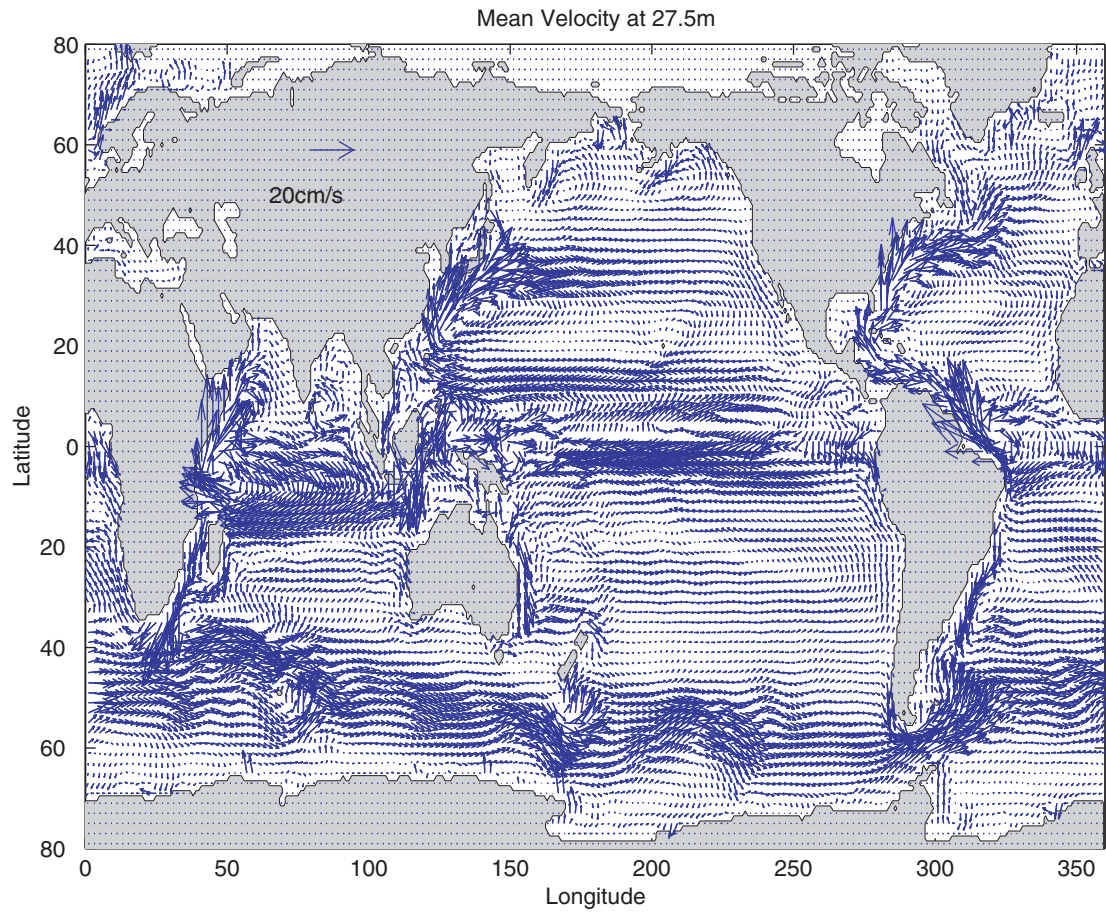
[29] We now turn to the results of the optimization procedure. These differ from either the model or the data alone and illustrate a three-dimensional time-evolving model that is mostly consistent (in the form described in section 6) with all data shown in Figure 3. The consistency is the result of modifications in the initial conditions and the daily NCEP surface forcing fields, and these adjusted fields must be regarded as part of the oceanic state. In a fully rigorous statistical context one would refer to the changes we estimated as “corrections.” However, because of the lack of a formal internal model error covariance and other remaining inconsistencies, we refer to them here as “adjustments.” A thorough analysis in terms of errors in the ocean model and the atmospheric analysis is described by *Stammer et al.* (submitted manuscript, 2002b). Because of remaining uncertainties in model physics, the surface forcing, and associated model drifts, one anticipates, a priori, a more accurate and precise estimate of the oceanic variability than of the absolute (time average) state. The ultimate adjustment time of the GCM is far longer than the 6-year interval over which data have been provided, and, formally, no information is provided to the optimization algorithm about the extent to which, for example, the real ocean is undergoing century-long drifts.

[30] Adjustments to the initial *Levitus et al.* [1994a, 1994b] January mean  $\theta$  and  $S$  fields are illustrated in Figure 5 from 5 and 435 m depth, respectively. Many structures in the changes can be associated with real interannual ocean variability, which renders the hydrography at the beginning of 1992 different from the climatological January values. That temperatures are changed in the model at 435 m and much deeper is important: It supports the inference that surface elevation (altimetry) reflects processes occurring deep within the ocean and that the altimeter provides a window into the ocean abyss.

[31] Temperature changes in the optimization can be summarized as a general warming of the subtropical gyres and in many of the boundary currents (the climatology is much too smooth there), while the tropical regime and high latitudes show predominant cooling. Note the strong salinity increase near the surface over high latitudes, especially in the Southern Ocean, while most of the remaining near-surface ocean is freshened. The opposite tendency can be found at depth.

[32] Mean changes of net surface heat and freshwater flux fields relative to the prior NCEP fields as they result from the optimization are displayed in the upper row of Figure 6. Modifications of the net NCEP heat fluxes are of the order of  $\pm 20 \text{ W m}^{-2}$  over large parts of the interior oceans. Maximum changes occur along the boundary currents in the Northern

**Figure 7.** (opposite) (a) Estimated mean SSH field (cm) as it results from 6-year assimilation period. (b) Estimated mean residual  $\bar{\eta}_e - \bar{\eta}_{lp}$  (cm). Note data gaps in tropical regions due to altimeter track pattern. All data over regions with water depth  $< 1000$  m were neglected here.



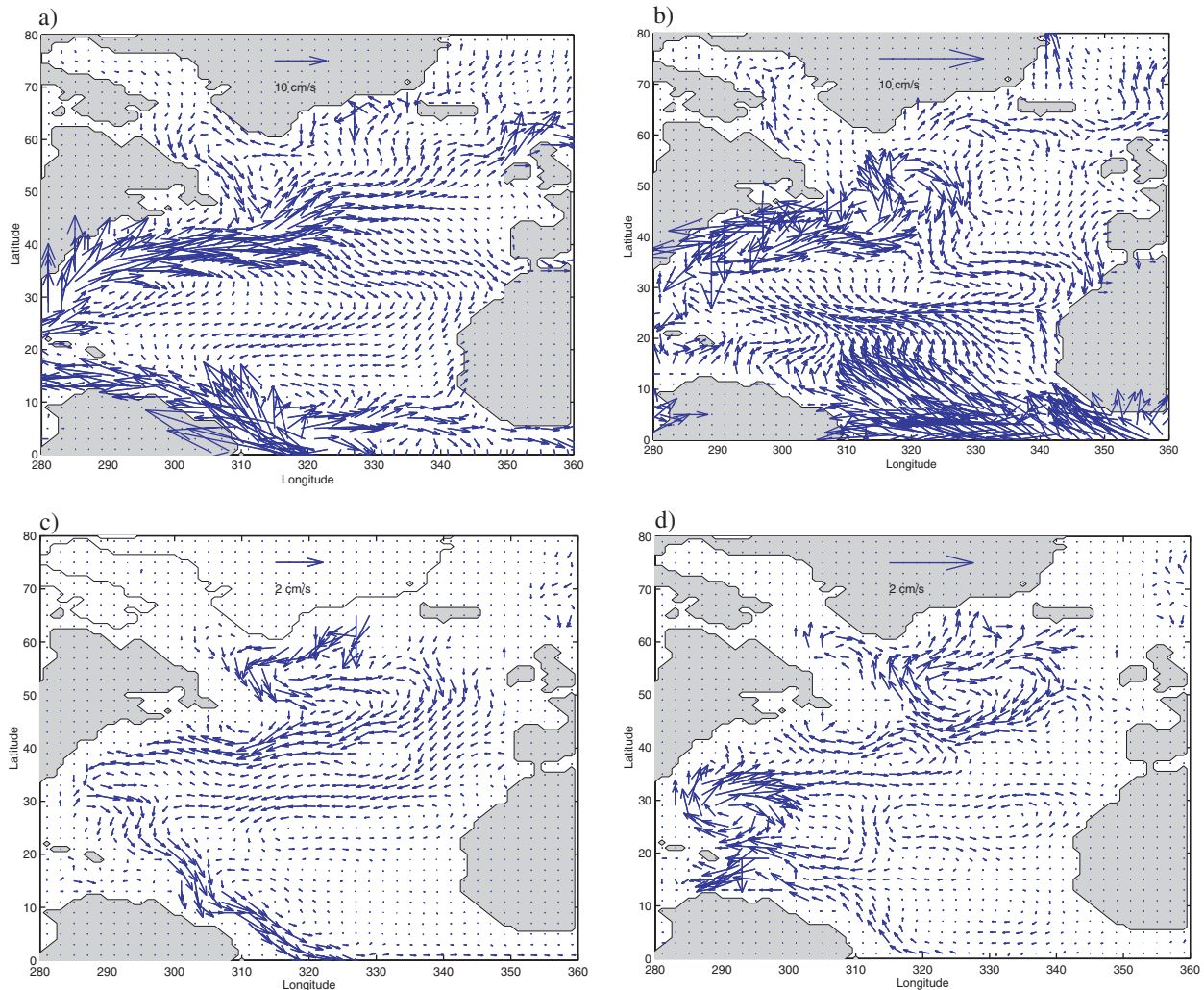


**Figure 9.** (a, b) Mean estimated velocity and (c, d) its differences relative to unconstrained models plotted from Atlantic at 27.5 m depth (Figures 9a and 9c) and at 1975 m depth (Figures 9b and 9d).

Hemisphere, where shifts of up to  $\pm 80 \text{ W m}^{-2}$  can be found. Most of the eastern boundary currents now show a significant heat uptake. The same is true in the Arabian Sea where, similarly, the offshore Ekman transport brings up cold water from below that is being heated by the atmosphere. Strong warming now occurs over Flemish Cap, in the North Pacific, and along most of the Antarctic Circumpolar Current (ACC). Note that the optimization removes some of the small-scale Gibbs effects, known to be present in the NCEP initial estimate buoyancy flux fields as a result of mountain ranges such as the Andes and visible in the eastern Pacific.

[33] Positive net evaporation minus precipitation ( $E - P$ ) values are directed into the atmosphere over the eastern side of all subtropical gyres. Large net precipitation can be found in the tropics, especially over the Pacific warm pool, and over most of the high latitudes. The biggest changes of  $E - P$  occur near the boundaries and can often be associated there with river discharge (e.g., in the Gulf of Bengal or near the Amazon Delta) or with ice import and ice melting

(e.g., over parts of the Labrador Sea) not properly represented in the prior  $E - P$  fields.

[34] The wind stress fields also adjust so as to better reproduce the observed oceanic fields (Figures 6c and 6d). As compared to the net heat and freshwater changes, smaller scales are visible in the modifications of the stress fields. The fact that their largest modifications exist close to intense boundary current systems indicates the difficulty that a model with  $2^\circ$  horizontal resolution has in producing the proper current separation without extra vorticity input by the modified wind stress. On the other hand, the increase of the trade winds over the tropical Pacific is consistent with the prior knowledge of NCEP errors there [Milliff *et al.*, 1999], and the adjustments are a true correction in that region (see discussion by Stammer *et al.*, submitted manuscript, 2002b).

[35] In summary, the changes in the initial  $\theta$ ,  $S$  fields and amplitudes of changes in the external forcing fields are, overall, consistent with accepted uncertainties in the hydrographic climatology and meteorological analyses. Some

**Figure 8.** (opposite) Mean estimated velocity fields from (a) 27.5 and (b) 1975 m depth ( $\text{cm s}^{-1}$ ) as they result from 6-year assimilation period.

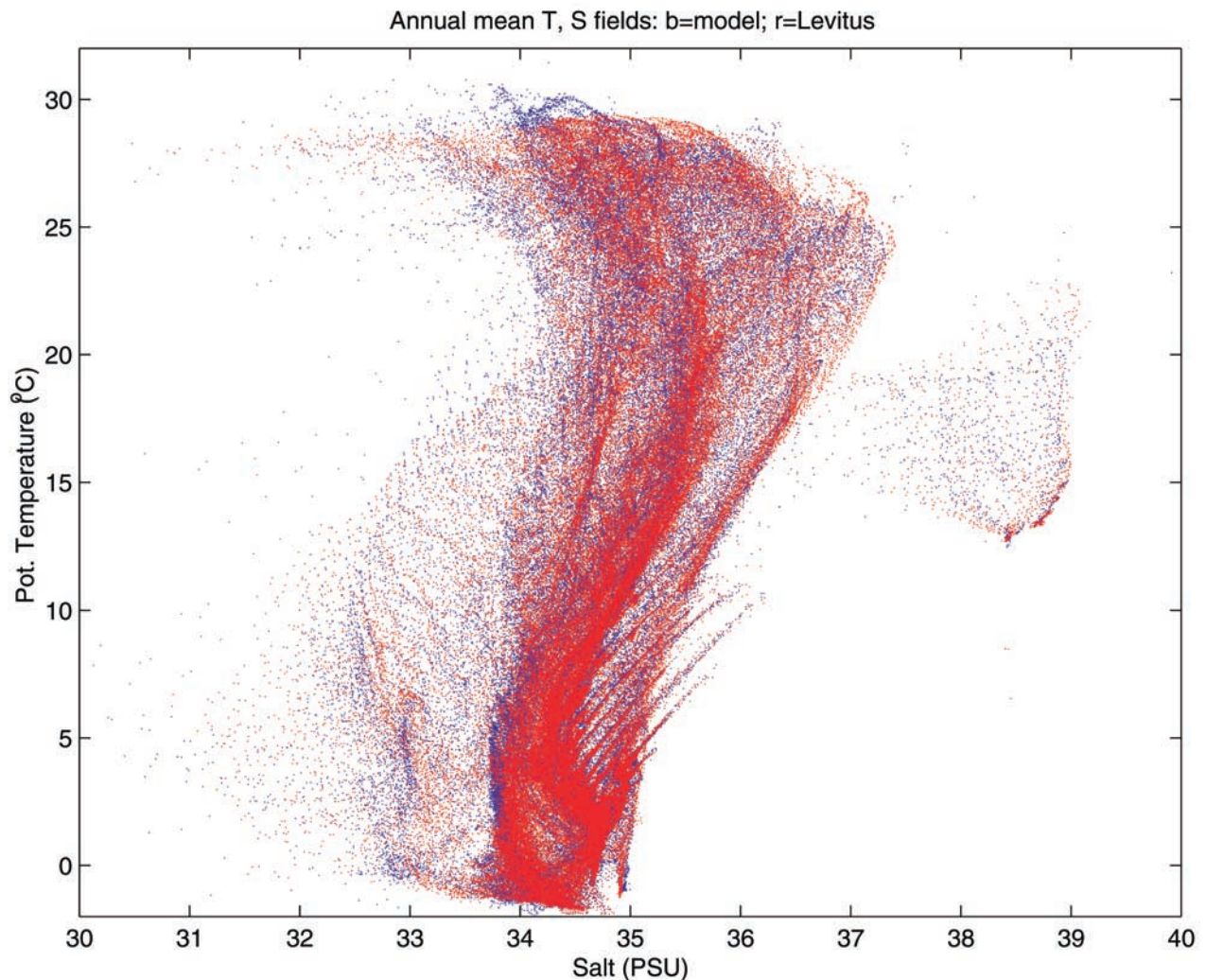


**Figure 10.** A  $\theta$ - $S$  diagram of 6-year mean model (blue) and climatological annual mean Levitus  $\theta$  and  $S$  fields (red).

changes in boundary forcing are clearly compensating for inadequacies in model resolution. By applying the estimated surface forcing fields to the model, the total model kinetic energy increases by  $\sim 15\%$  compared to the reference run.

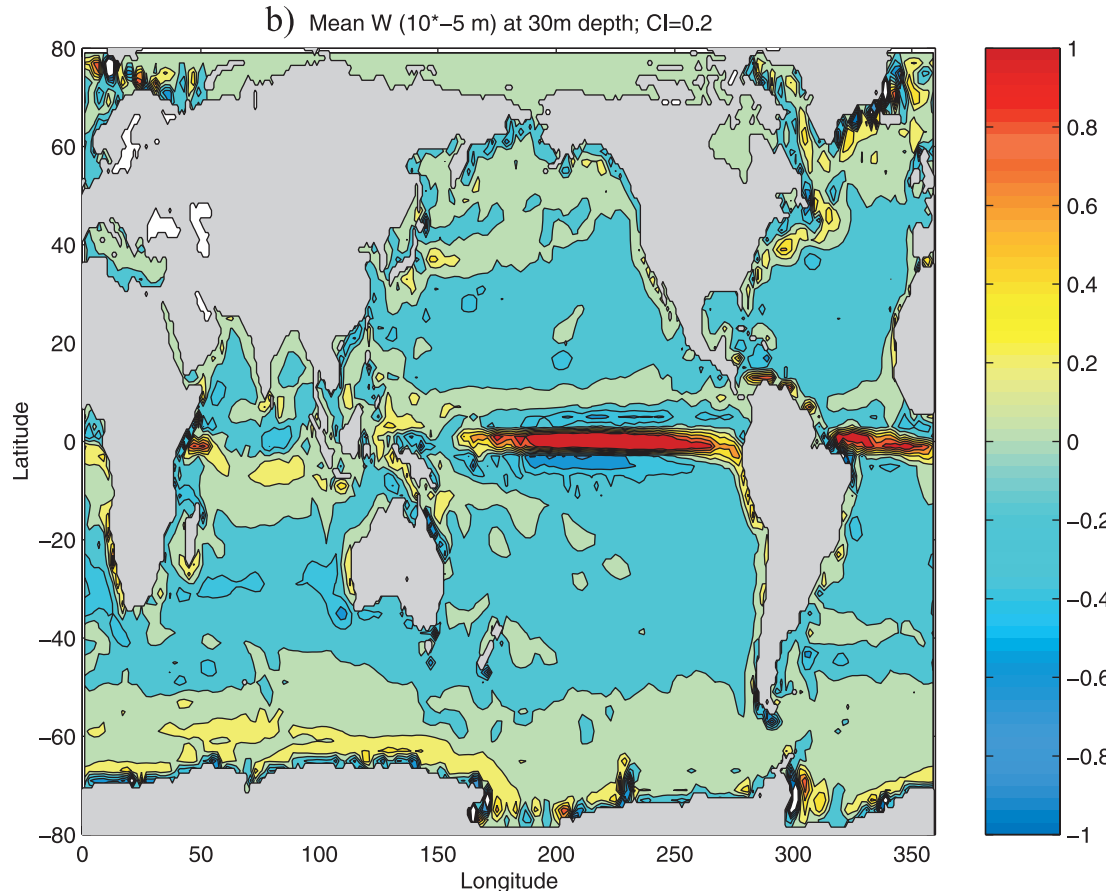
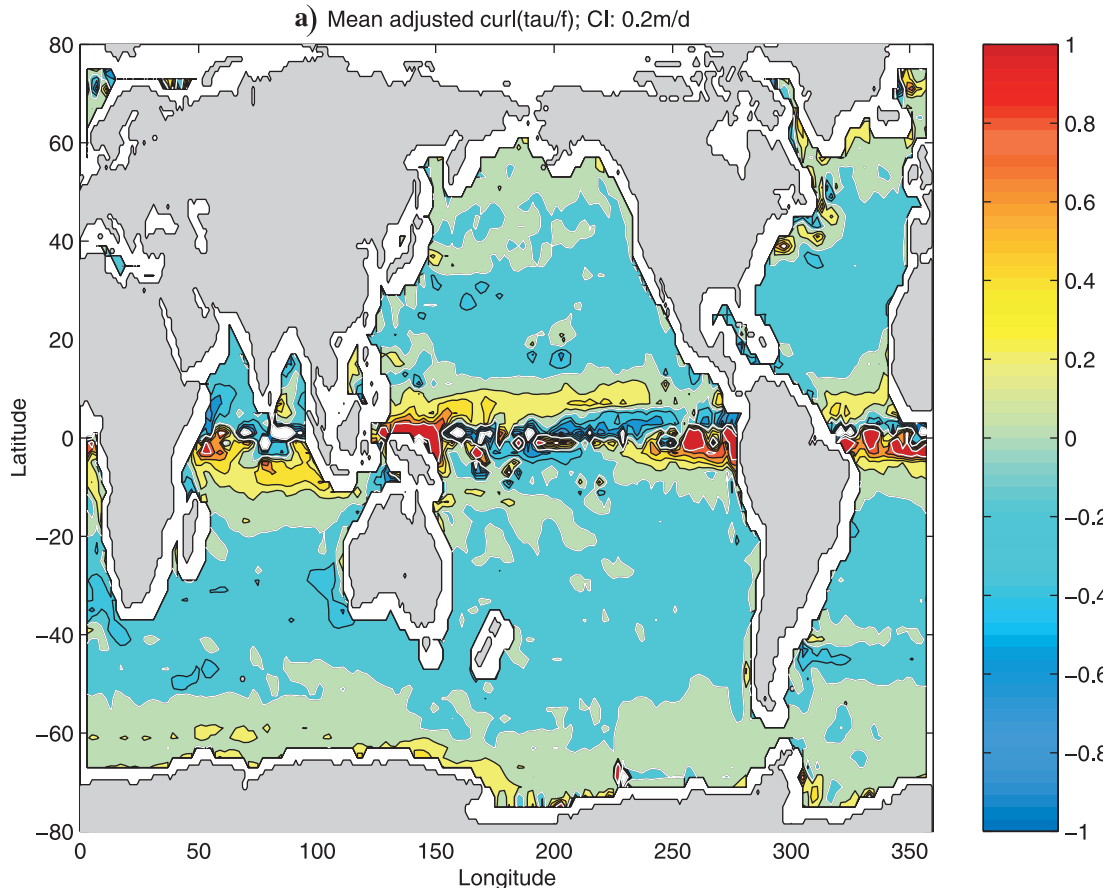
#### 4.1. Mean State

[36] As already noted, there are reasons to anticipate that the mean state of the model could not be fully in accord with known physics. Nonetheless, the constrained model is closer to the SSH and hydrographic observations than is the control run (see below), and there is no evidence that any significant element has become less realistic.

[37] In Figure 7a we show the estimated mean sea surface height field as it results from the 6-year period. The associated velocity fields from 27.5 and 1750 m depth are shown in Figures 8a and 8b, respectively. All major current systems are present, but with the present low model resolution, they are necessarily overly smooth.

[38] On smaller scales, eddy-like features (at the long-wavelength extreme) become visible, for example, in the Gulf of Bengal, as the Great Whirl in the Arabian Sea, and even in the Caribbean. In the North Atlantic a deep western boundary current is present along the entire meridional extent of the Atlantic Ocean, with significant sources coming from east of the Mid-Atlantic Ridge over large parts of the North Atlantic basin. Maximum strength of the deep western boundary current in the Atlantic Ocean is located below the layer shown and was chosen to provide a more complete picture in the Pacific and Indian Oceans. At that greater depth in the Pacific, there is a much weaker, but quite similar deep western boundary current in the Northern Hemisphere and a quite strong, deep southward flowing western boundary current in the Southern Hemisphere. However, these flows are discontinuous, being separated by a westward flow along the equator at this depth. However, the equatorial resolution in the model is not adequate

**Figure 11.** (opposite) (a) Ekman pumping velocity,  $w_E = \text{curl}(\tau)/f$ , as it results from the mean estimated wind field. Mean vertical velocity at (b) 37.5 and (c) 1750 m. Contour interval is  $0.2 \times 10^{-5} \text{ m s}^{-1}$ .



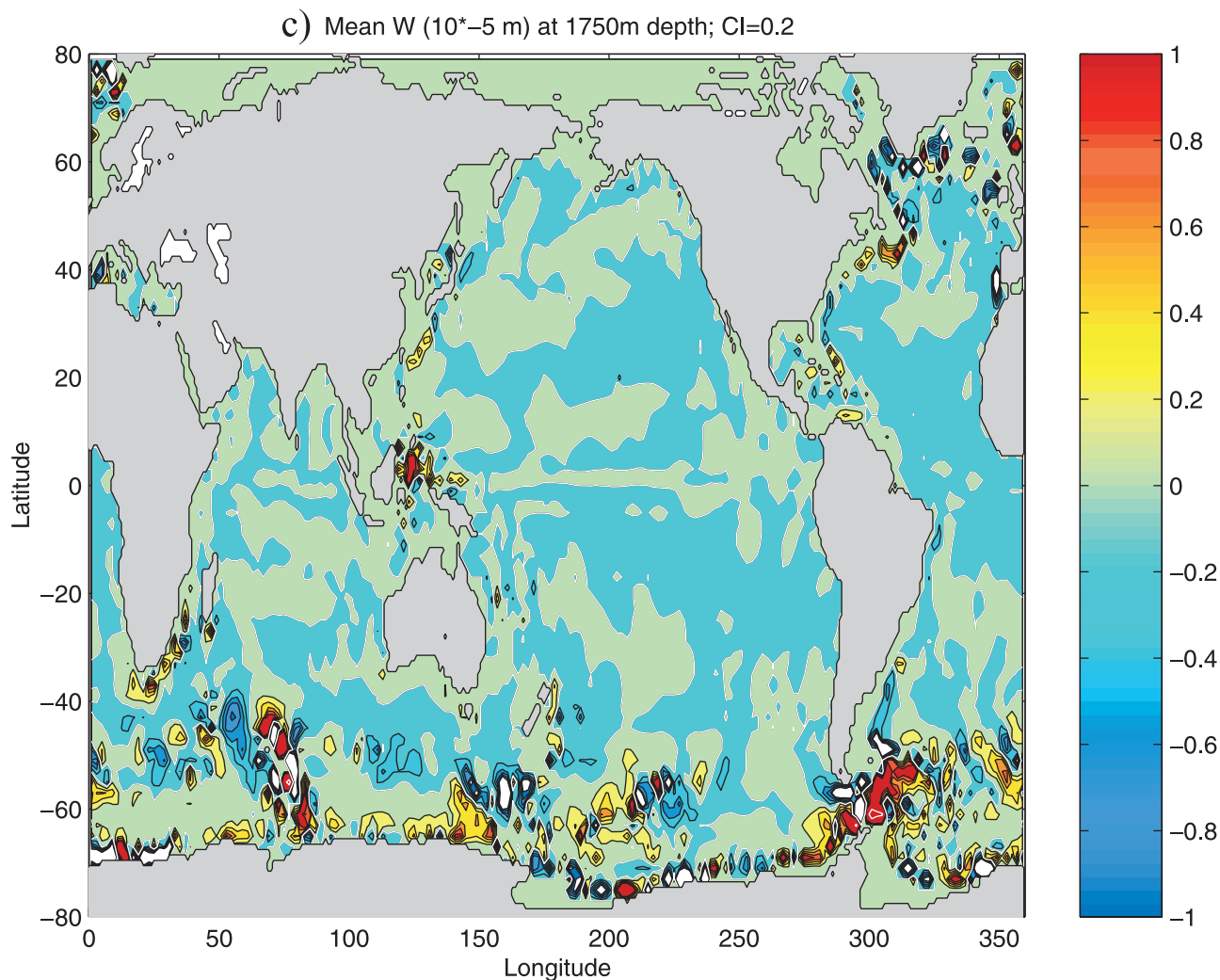


Figure 11. (continued)

for providing a detailed picture there. Note also the deep western boundary current present in the Southern Hemisphere of the Indian Ocean.

[39] To illustrate the estimated flow field and its change relative to the first guess in more detail, Figure 9 shows results from the North Atlantic Ocean. The estimate has a much enhanced flow field associated with the Gulf Stream and its extension, including the Azores Current and the anticyclonic circulation associated with the Northwest Corner. These features are very poorly simulated in most coarse-resolution numerical models. Here the assimilation procedure is able to largely correct for the traditional shortcomings by changing the surface boundary conditions. (Whether erroneous surface meteorology is indeed the cause of much of the traditional difficulty is an example of the model versus observation error dichotomy requiring further information to resolve.) A marked increase in the volume of slope water north of the Gulf Stream leads to a better current separation there. At depth it appears that the deep western boundary current is mostly weakened, as is the subpolar gyre strength.

[40] In many previous model simulations the resulting  $\theta$ ,  $S$  structures were quite different from those observed [cf. *Klinck, 1995*]. However, the estimated  $\theta$ ,  $S$  structures here

preserve the basic water mass distributions within uncertainty limits and with uncorrelated  $\theta$  and  $S$  residuals (Figure 10). A further test of the consistency of RMS differences between estimated and climatological fields with prior  $\theta$ ,  $S$  errors is described below.

[41] The Ekman pumping velocity,  $w_E = \hat{\mathbf{k}} \cdot \text{curl}(\boldsymbol{\tau})/f$ , is displayed in Figure 11a as it results from the mean estimated wind field. For comparison, the mean vertical velocity in the model is shown in Figures 11b and 11c at 37.5 and 1750 m depth, respectively. In the tropics, there are clear indications of Ekman convergence and equatorial upwelling, and the general pattern of the near-surface vertical velocity over the bulk of the ocean shows large-scale Ekman pumping and suction regimes. At depth, however, the upwelling and downwelling patterns are complex, and far from spatially uniform, showing the clear impact of topographic features. In particular, we find the largest vertical velocity amplitudes along boundaries, irrespective of depth, especially in the North Atlantic and in the ACC region. We will discuss elsewhere the relationship to theories of the abyssal circulation.

[42] An important indicator of exchange processes with the atmosphere and of internal water mass conversion



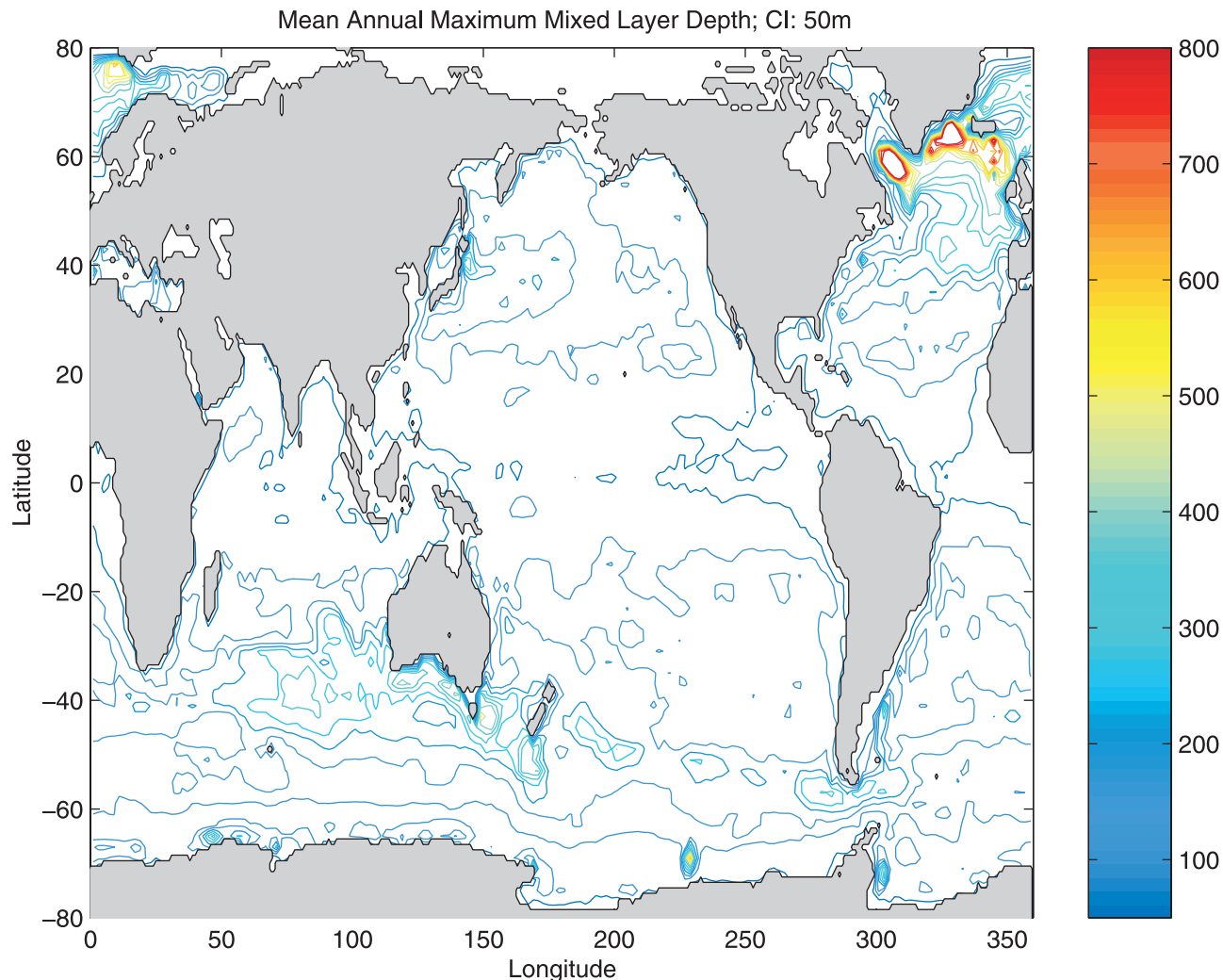


**Figure 12.** Annual maximum mixed layer depth (m) as it results from KPP [Large *et al.*, 1994] mixed layer model.

mechanisms is the wintertime mixed layer depth, which is shown in Figure 12 as the annual maximum. Deepest reaching convection occurs in the North Atlantic, where levels of  $\sim 1500$  m are reached. General mixed-layer structures are qualitatively consistent with observations [e.g., Woods, 1984], but the mixing and  $18^\circ$  water mass formation in the vicinity of the Gulf Stream extends somewhat too far south. Note the deepest convection occurring over most of the eastern North Atlantic and over large parts of the Norwegian Sea. The area of the eastern subtropical Atlantic shows enhanced winter deepening as compared to the surrounding areas. Estimated mixed layer depth values of 200 m are consistent with the results of Spall *et al.* [2000] in that region. Other regions of enhanced convection can be found near the Kuroshio, over most subtropical gyres in the Southern Hemisphere, and along the ACC, especially upstream of Drake Passage and in the Indian Ocean. Most of those regions coincide with areas of net surface cooling (not shown, but see Stammer *et al.* (submitted manuscript, 2002b) and point to the net surface buoyancy forcing as a primary (but not necessarily local) cause of deep convection in the model. Enhanced wintertime mixing occurs also in

the Sea of Japan and in the eastern Mediterranean, where the Levantine Intermediate Water is formed.

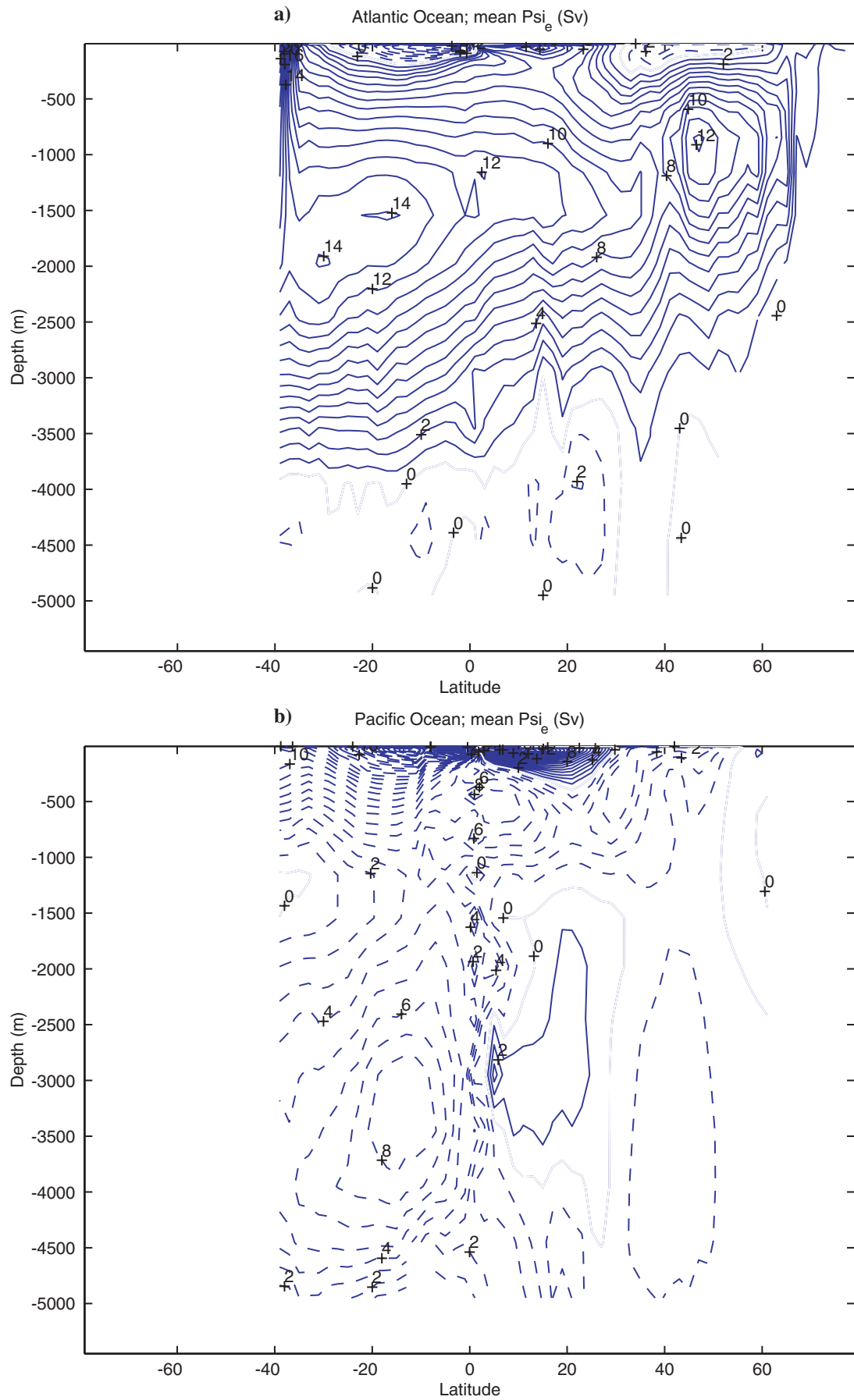
#### 4.2. Meridional Mass Transport Stream Function

[43] The time-mean meridional mass transport stream function,

$$\Psi(y, z) = \int_{-H}^{\eta} \int_{0(y)}^{L(y)} v(x, y, z) dz dx, \quad (6)$$

is plotted in Figure 13 for the Atlantic, Pacific, and Indian Oceans. Fields were evaluated for the last 5 years of the assimilation period, omitting the first year to avoid initialization transients in  $\Psi$  arising from adjustment to changed  $\theta$ ,  $S$  initial conditions.

[44] In the North Atlantic (Figure 13a),  $\sim 15$  Sv of North Atlantic Deep Water (NADW) are produced, of which  $\sim 4$  Sv are being upwelled around  $40^\circ$ N at the western boundary. The remaining 11 Sv leave the Northern Hemisphere, but entrain more water on their way south, leading to 16–18 Sv being injected into the ACC area. About 2 Sv of Antarctic Bottom Water (AABW) flows northward in the Atlantic, originating south of the ACC.



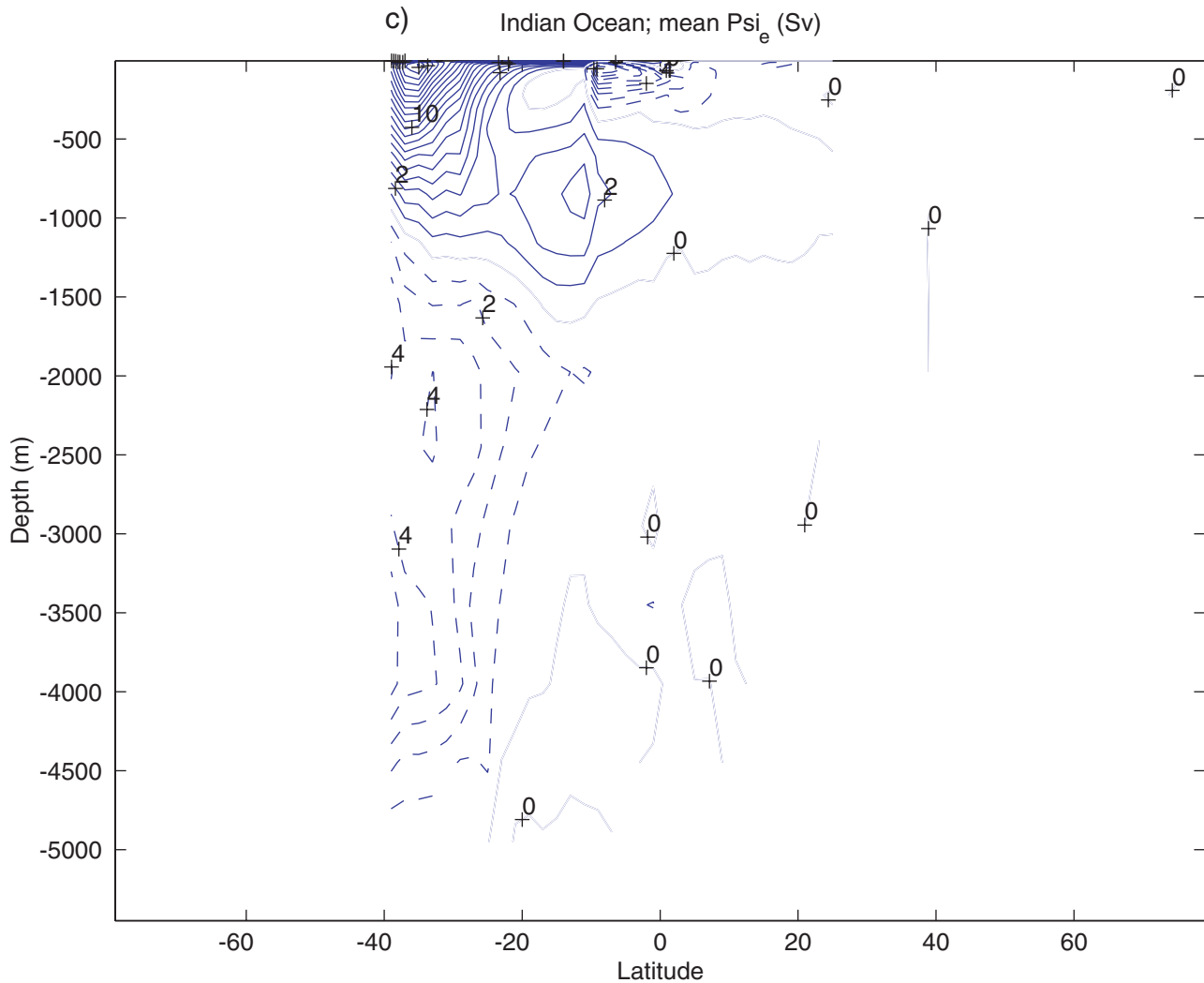


**Figure 13.** (continued)

[45] A substantially larger inflow exists for the Pacific and Indian Oceans (Figures 13b and 13c), which show a large upwelling cell below 2000 and 1000 m depth, respectively, with most of the upwelling occurring south of the equator. In the North Pacific a similar but reversed cell is present. The temporal variability of  $\Psi$  is very large and is of the same order or greater than its mean value. Maximum variability can be found in low latitudes and around the ACC.

## 5. Seasonal to Interannual Variability

[46] We begin with the seasonal and lower frequencies. Longitude-time plots along the same section as shown in Figures 1 and 2 are given in Figure 14, but from the constrained model. Results are visually similar to the T/P data. However, the general variability level is lower than is observed by T/P, as one expects with a non-eddy-resolving

model. Differences are associated with an apparent eastward moving pattern along  $30^\circ\text{N}$ , which is only weakly represented in the altimeter data.

[47] The bulk of the energy at the annual cycle is associated with the seasonal heating and circulation changes [cf. Wunsch and Stammer, 1995, Plate 3]. Amplitude and phase of the annual harmonic of SSH and of the vertically integrated heat content in the model are shown in Figure 15. Both amplitude and phase are similar to the observations, especially in midlatitudes and in the Indian Ocean. Differences between the amplitudes are largest in the eastern tropical Pacific, owing to the interannual and ENSO-related variability there, and in the ACC. At the latter location, there is a noteworthy difference in the phases of the SSH and heat content annual harmonics in the Southern Ocean upstream of Drake Passage that appears also but is less pronounced in the annual harmonic amplitudes. This region has been identified before as one of

**Figure 13.** (opposite) Mean meridional mass transport stream function evaluated over (a) Atlantic sector, (b) Pacific sector, and (c) Indian Ocean sector.

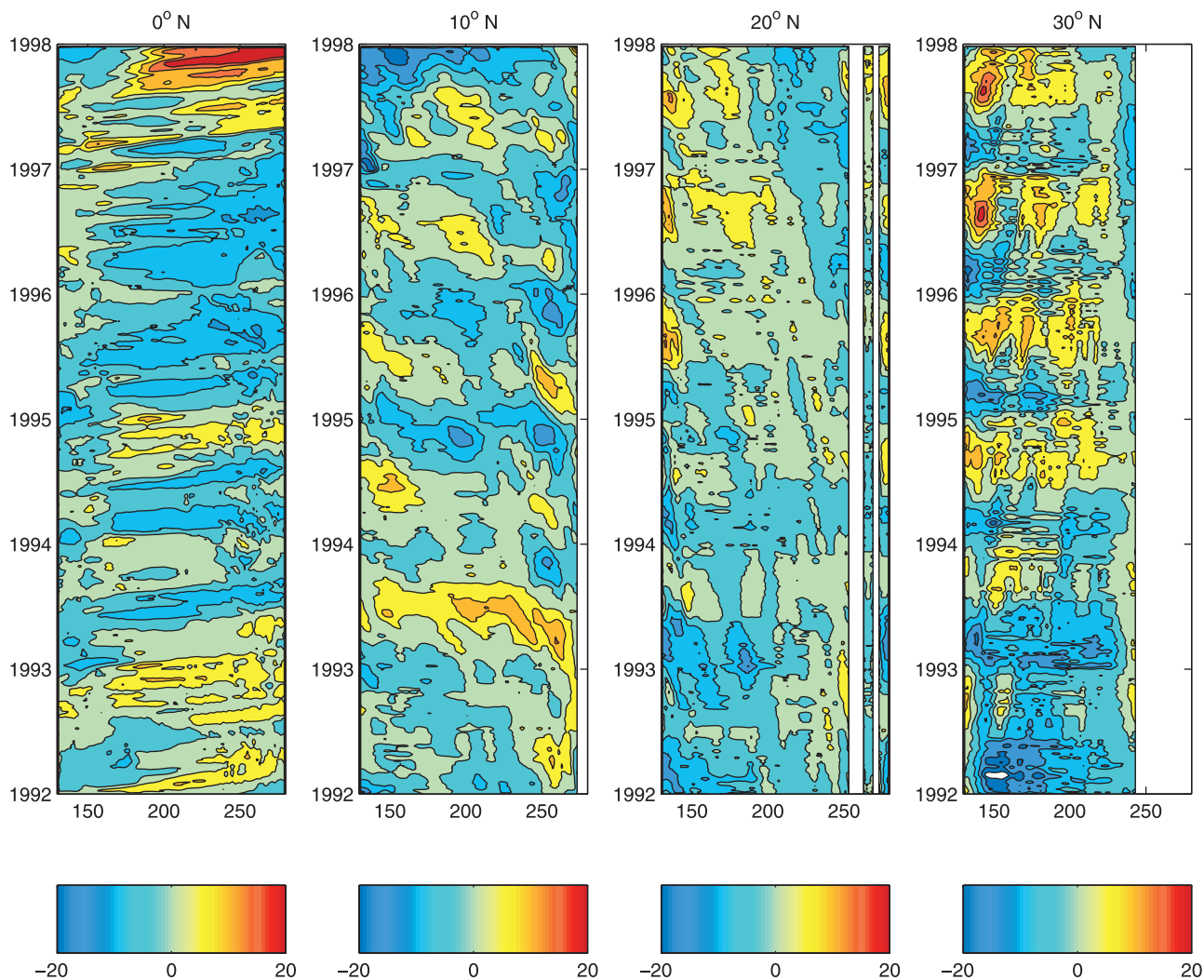


**Figure 14.** Longitude-time sections for SSH anomalies in constrained model for, from left to right,  $0^{\circ}\text{N}$ ,  $10^{\circ}\text{N}$ ,  $20^{\circ}\text{N}$ , and  $30^{\circ}\text{N}$ . Displayed fields were smoothed over 10 days to suppress vigorous barotropic signal that would otherwise dominate.

vigorous barotropic variability in the T/P data [e.g., *Fukumori et al.*, 1998; *Stammer et al.*, 2000]. The differences in the amplitudes and phases of the annual harmonics imply that much of the SSH variability at the annual period is associated there with mass redistribution rather than with steric (heat content) changes. *Ponte et al.* [2001] discuss the annual harmonic of the bottom pressure and the corresponding surprisingly intense barotropic circulation of the global ocean. In midlatitudes, phase fields show mostly the seasonal heating and cooling cycle. Low latitudes are very different, however, where the changes in the wind field introduce a rapid dynamical response of SSH and temperature at this period.

[48] Of considerable interest is also the annual harmonic of the sub-surface flow and temperature and salinity fields, especially in low latitudes and in the Indian Ocean. Figure 16 shows the anomalies of the velocity and temperature fields as they emerge at the annual period at 610 m depth. Only the September anomalies are shown; March anomalies are similar, but with opposite signs. The low latitudes dominate the changes in the flow field, but variations of comparable

amplitude are also present in midlatitudes, especially in the Kuroshio/Oyashio regime, where previous studies indicated a measurable contribution of changes in barotropic transports to annual SSH anomalies [e.g., *Chelton and Mestas-Nuñez*, 1996; *Stammer*, 1997]. Note also the relatively strong response of the flow field all along the southeastern coast of Australia and connecting from there well into the tropical Indian Ocean.

[49] Temperature anomalies at the annual period mostly coincide with those in the flow field, especially in the eastern tropical Pacific and Indian Oceans, where they show Rossby wave structures with amplitudes as large as  $0.1^{\circ}\text{C}$  or more at 600 m depth. These structures are consistent overall with advective processes of the anomalous flow field. But even in the subtropics and higher latitudes, we encounter similar amplitude anomalies. Some of these arise from deep convection events, for example, near the Gulf Stream extension or over the Agulhas region. However, some can also be associated with changes in frontal structures, for example, near the Kuroshio Extension.

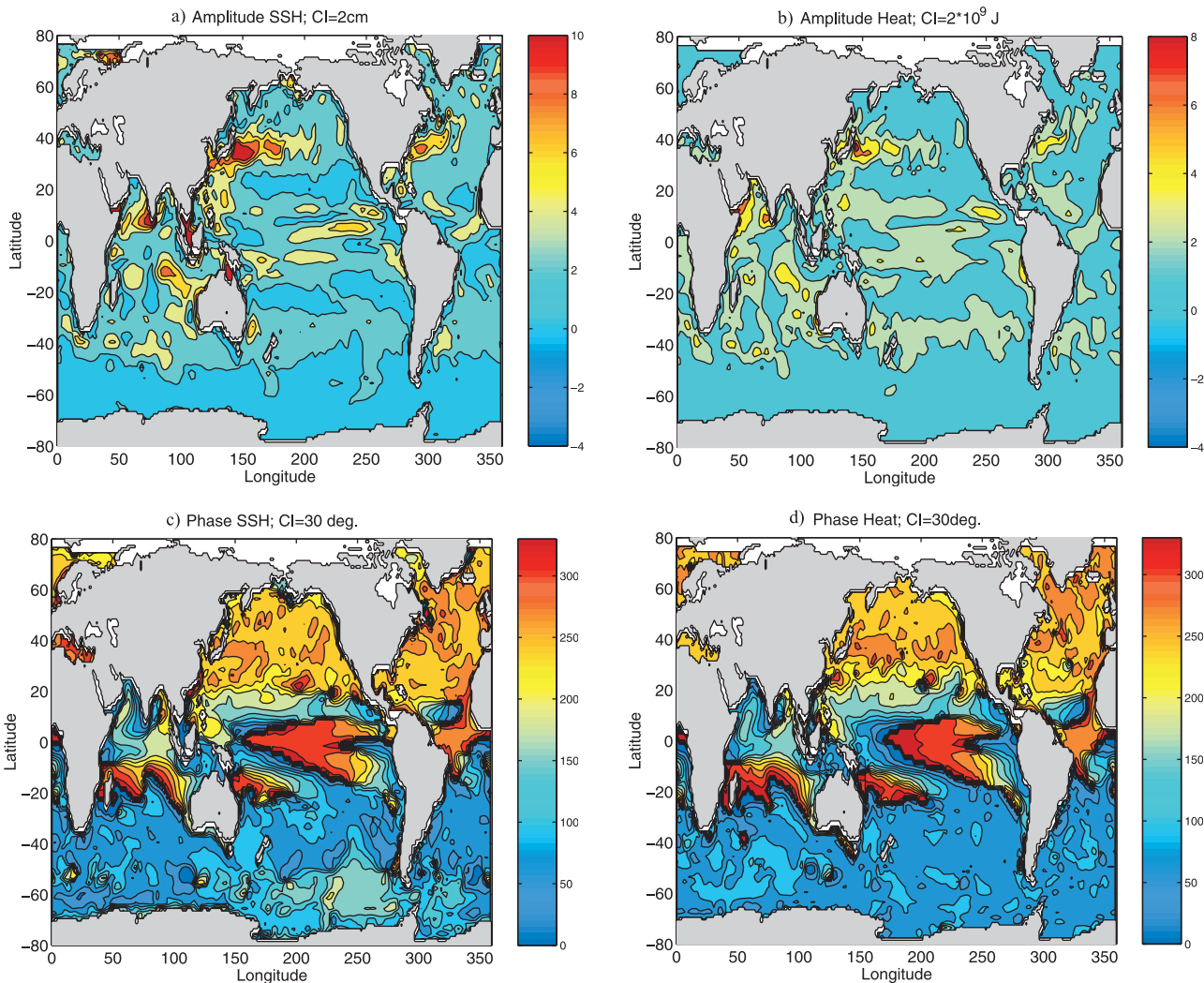


**Figure 15.** (a) Amplitude and (c) phase of annual harmonic of SSH (in centimeters and degrees relative to 1 January) and (b) amplitude and (d) phase of vertically integrated heat content in model (in Joules and degrees relative to 1 January).

[50] The eddy-like features in the annual harmonic figures to some extent can be aliased features, although they could also be caused, in principle, by a local convection feature. However, the maximum mixed layer depth does not show any related structure. Note that the eddy features do not show up in the velocity map, but characterize the temperature, heat, and surface height figures along the ACC and in the North Atlantic and North Pacific.

## 6. Testing Results

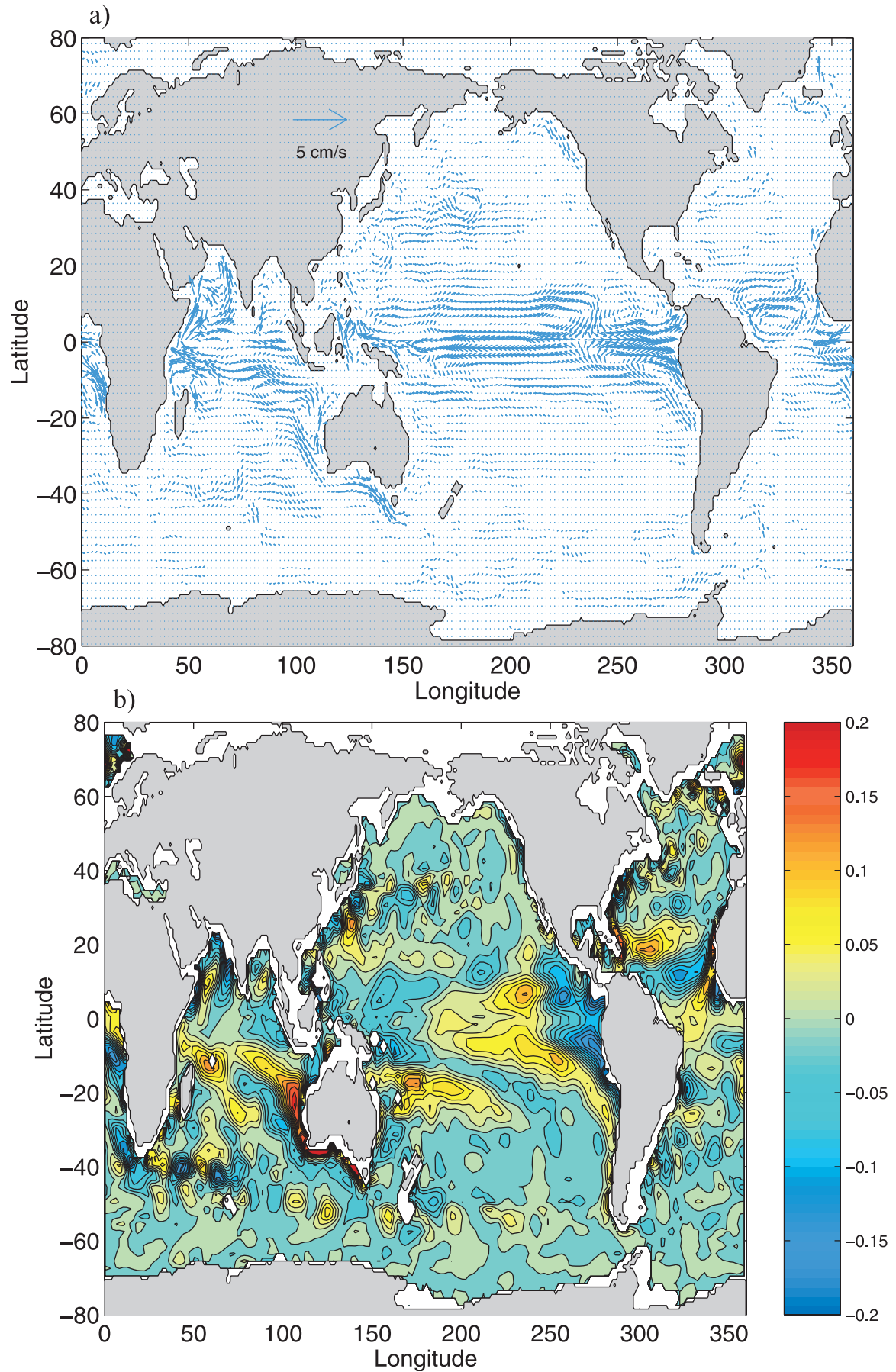
[51] Any quantitative estimation procedure requires a detailed posterior test of the results and their consistency with prior error assumptions. This step includes the computation of formal uncertainties. However, because the calculation of error bars is currently beyond what is computationally possible, we undertake here to test the results by systematically comparing them with some of the data that were used as constraints and with data withheld from the calculation. In future calculations the withheld data, if statistically consistent with the present assimilated state,

will be added to the calculation, thus further constraining the system.

### 6.1. Mean Surface Height Residuals

[52] The estimated mean residual  $\bar{\eta}_e - \bar{\eta}_{tp}$ , which is the difference between EGM96 and the geoid implied by the time average ocean circulation and T/P, displayed in Figure 7b, shows amplitudes on the order of  $\pm 10$  cm over large parts of the ocean. Residuals up to  $\pm 50$  cm exist, however, in some locations, notably along most island arcs (e.g., the Aleutian Trench, in the Caribbean and the Indonesian Archipelago, Hawaii, and the Emperor Sea Mount Chain, near Bermuda, etc.) and in the vicinity of topographic features along the ACC, for example, south of New Zealand. The average (RMS) error is acceptable, but there are significant outliers, too large to be consistent with the prior error statistics of  $\sim 5$  cm or less (see Figure 4).

[53] Some structures in the residuals mimic the flow field itself, for example, the Gulf Stream, the Kuroshio, the subtropical gyre in the South Atlantic, etc., and could therefore point toward problems in the simulated mean



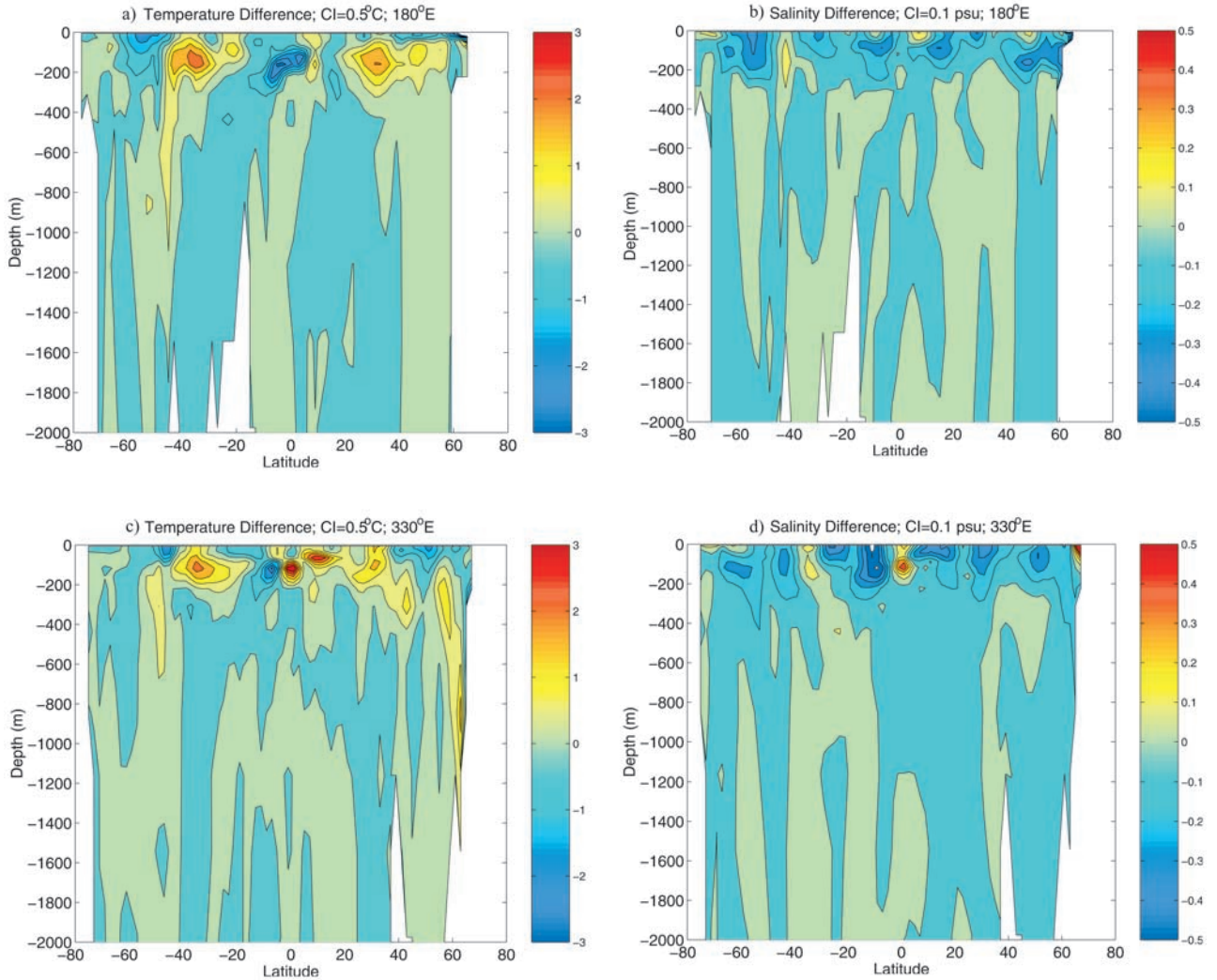


**Figure 17.** Differences between mean-over-6-years estimated  $\theta$ ,  $S$  fields and those from *Levitus et al.* [1994a, 1994b] climatology along meridional sections at (a)  $180^\circ\text{E}$  and (c)  $330^\circ\text{E}$  longitude. Differences between mean estimated  $S$  field and that from *Levitus et al.* [1994a, 1994b] climatology at meridional sections along (b)  $180^\circ\text{E}$  and (d)  $330^\circ\text{E}$  longitude. All sections are displayed only over top 2000 m depth.

circulation. However, the close association of most large residuals with topographic features and their resemblance to independent estimates of the EGM96 error [Pavlis *et al.*, 1999] suggests that we are seeing, primarily, geoid errors in excess of those formally estimated for EGM96. To test this hypothesis, we have used the model results to construct a new geoid by subtracting the mean estimated SSH field (of an earlier but nearby solution) from the mean T/P absolute SSH observations. N. Pavlis *et al.* (personal communication, 2000) used the resulting estimate to calculate the T/P and other satellite orbits. The resulting orbit ephemerides are at least as good as those based on more conventional geoids, and for some satellite missions, they are actually superior to those obtained from EGM96. Our tentative conclusion here is that the more extreme residuals we see between the a priori estimated sea level ( $\eta_{\text{T/P}}$ ) and that resulting from the

assimilation are consistent with their being geoid errors, and the hypothesis of a dominating model error is not required to explain the time-mean SSH residuals.

## 6.2. Mean Temperature and Salinity Fields

[54] The model was constrained to stay close to the *Levitus et al.* [1994a, 1994b] monthly climatological hydrographic  $\theta$  and  $S$  fields within error bounds (see Figure 4a). Here we will first test the resulting mean  $\theta$ ,  $S$  fields against the “Levitus climatology” and its a priori error. Then we will further test the assimilation against the withheld WOCE hydrography.

[55] Differences between the mean-over-6-years estimated  $\theta$ ,  $S$  fields and those from the climatology are shown in Figure 17 from meridional sections along  $180^\circ\text{E}$  and  $330^\circ\text{E}$  longitude. Above 100 m the assimilation produces

**Figure 16.** (opposite) (a) Velocity ( $\text{cm s}^{-1}$ ) and (b) temperature ( $^\circ\text{C}$ ) anomalies at annual frequency plotted for September at 610 m depth. Vectors with magnitude  $<0.1 \text{ cm s}^{-1}$  were not plotted. Contour interval for temperature map is  $0.02^\circ\text{C}$ .

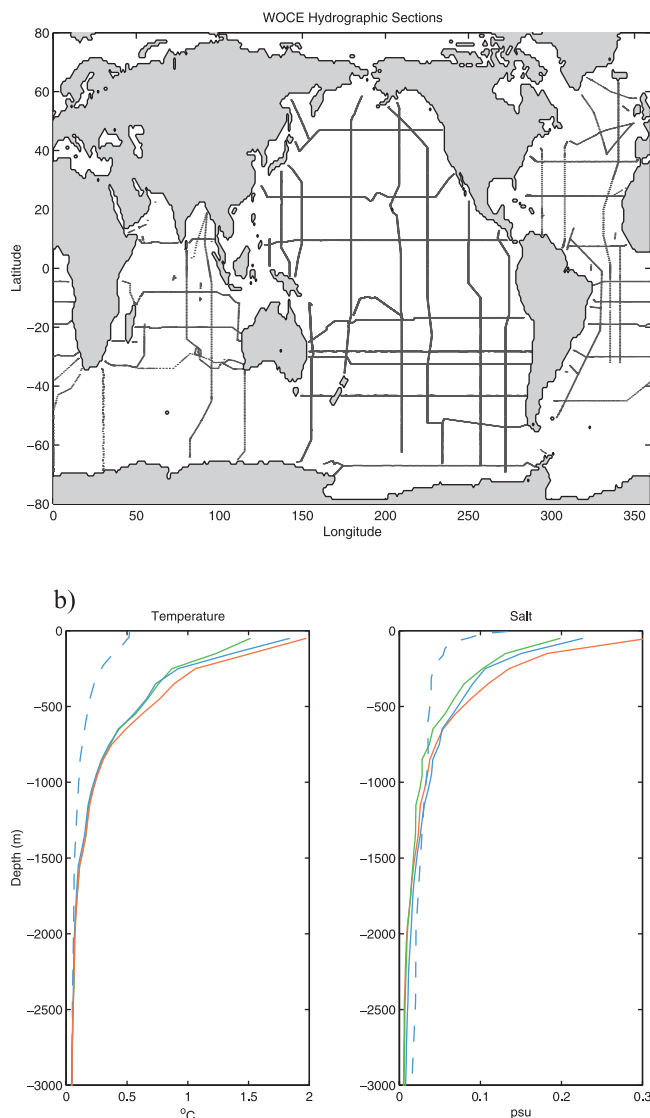


**Figure 18.** (a) Locations of World Ocean Circulation Experiment (WOCE) one-time hydrographic sections used in this study. (b) RMS differences computed along all WOCE sections and between WOCE data and unconstrained model run (red), constrained model (blue), and Levitus annual mean fields (green). Dashed blue curve shows prior error prescribed for Levitus fields, displayed also in Figure 4.

temperatures generally lower than in the climatology. Below the region of reduced temperatures the values are slightly increased in the assimilation, although not uniformly so. Taken together, these results hint at a weakening of the thermocline in the model by downward diffusion of heat. Further down in the water column, differences relative to the climatology are substantially smaller, but are still significant over the entire Southern Ocean and along lateral boundaries.

[56] For salinity, the residuals show more structure visually correlated with the flow and gyre structures. Note, particularly, the signature of the tropical Pacific and Atlantic, the subpolar North Pacific, and along the ACC. The northern

North Pacific is colder and saltier near the surface, but is fresher and warmer at depth relative to the climatology. The North Atlantic is fresher and colder almost throughout (with smaller-scale deviations), while, near the surface, the ACC is fresher and saltier north and south of the ACC axis, respectively, with a reversal of this pattern at depth.

[57] To compare the estimation results to independent information not employed in the estimation process, we use here a large part of the global WOCE and pre-WOCE one-time hydrography depicted in Figure 18a [Koltermann *et al.*, 2002; Talley, 2002a, 2002b]. Because several of the sections shown in Figure 18 are from outside our estimation period, we compare them all to the model time-mean and also to the Levitus climatology.

[58] Differences between the Levitus climatology and WOCE data, on the one hand, and the model results and the WOCE data, on the other hand, are summarized in Figure 18b in terms of RMS differences computed along all WOCE sections. Also shown in Figure 18 are the prior errors of the climatological Levitus fields, as they were prescribed in the estimation. For  $\theta$  and  $S$ , a clear improvement can be found in the top 500–1000 m. Here the RMS differences between WOCE fields and climatology are as large as those obtained relative to the constrained run, and both are significantly larger than the prescribed error information. Below  $\sim 1000$  m depth all three curves remain close, and are consistent with the prior error field. Note that for salinity, the errors of the constrained model are slightly larger than those between the climatology and the unconstrained model, implying that the estimated initial salinity fields at depth are moving away from the WOCE sections. They are still consistent within error bounds, however. Note also that near the surface the climatological temperature is actually closer to the WOCE data than to either of the model solutions. Near-surface temperature differences are larger than prior error estimates by a factor of 3. A significant part of that error, however, arises because the WOCE sections do not reflect annual mean conditions. In addition, the large eddy variability present in the WOCE measurements produces large differences, particularly in the upper ocean. We infer that uncertainties in the climatologies over the top 1000 m may have been underestimated by a factor of 3 in the estimation procedure. Below that depth, there is no indication of inconsistency.

### 6.3. Comparison With Time-Varying XBT and Tropical Atmosphere–Ocean Data

[59] Although monthly mean SST fields are assimilated, most of the time-varying signal in the solution is being provided by the T/P and ERS altimeter data. To test the impact of these latter fields on the model state, we shift here to the time-dependent portions of the estimated temperature field, which can be compared directly to the XBT and temperature time series obtained by the Tropical Atmosphere–Ocean (TAO) array [McPhaden *et al.*, 1998] (see Behringer [1994] for an earlier comparison between altimetry and XBT-derived estimates). The XBT/TAO sampling during 1992–1997 is shown in Figure 19a.

[60] To obtain a measure of improvement in the estimates compared to the unconstrained model, Figure 19b shows the RMS difference as a function of depth, evaluated over the entire model domain and over the full 6-year period. RMS



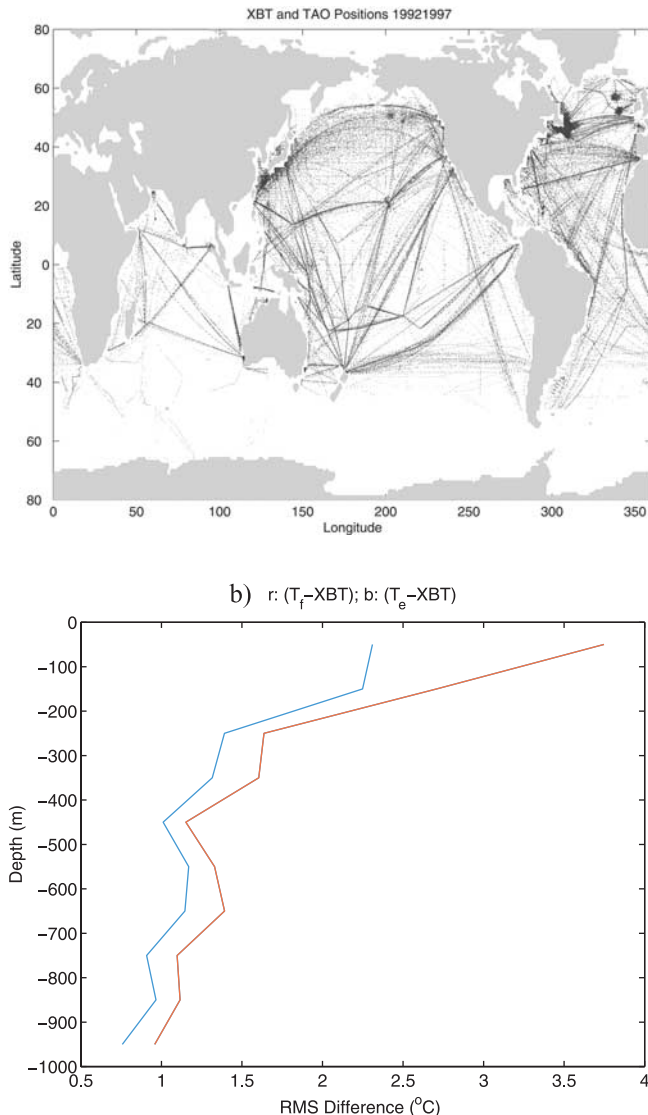


**Figure 19.** (a) Available expendable bathythermograph (XBT) data sampled over world ocean during 1992–1997; also included are data from Tropical Ocean-Global Atmosphere/Tropical Atmosphere-Ocean (TOGA-TAO) buoy network. Note that TOGA-TAO buoy data are included here in near-equatorial Pacific. (b) Global and time-averaged RMS difference as a function of depth of XBT data minus estimate (blue line) and minus control run (red line).

values of the XBT data minus the estimate (blue line) and minus the unconstrained forward model results (red line) are displayed. For this purpose, model fields were interpolated from monthly mean fields to XBT positions, both in space and time. Differences between XBT and estimated fields have decreased, compared to the unconstrained model, over the entire depth range by  $\sim 20\%$  and nearer the surface by  $\sim 30\%$ .

[61] As expected, the RMS differences between the estimate and the XBT/TAO data show a substantial spatial structure (Figure 20). The fields were computed as RMS differences within 10deg regions horizontally and within

various 100-m thick depth levels in the vertical. Near the surface, differences indicate deficiencies in the seasonal mixed layer of the present model. Farther down in the water column, however, enhanced RMS differences can be found along the path of major current systems. While the error is quite small in the quiet eastern regions ( $<0.5^\circ\text{C}$ ), the larger errors over the western basins are likely indications of mesoscale motions present in the XBT observations. However, a lateral shift or weakening of frontal structures in the model would appear as a similar structure.

[62] To illustrate the degree by which the error is being reduced by the data assimilation, we show in Figure 20b the difference between the fields provided in Figure 20a and similar ones based on the unconstrained model results. The reduced misfit upon data assimilation is negative in a few locations, indicating that the results from the constrained model are degraded there. However, the misfit reduction is mostly positive and in many places is as big as  $1.5^\circ\text{C}$  near the surface, and is even as big as  $0.5^\circ\text{C}$  at 600-m depths.

## 7. Summary and Conclusions

[63] The most important result from this experiment is the demonstration that it is now feasible to obtain estimates of the time-dependent ocean circulation by combining ocean observations with a numerical model using methods that are, in principle, fully rigorous statistical estimators. Through this procedure, it is possible to obtain three-dimensional oceanic state fields every few days and to obtain the associated surface forcing fields that are consistent with the global in situ and altimetric observations, SST data, atmospheric estimates of air/sea fluxes, and the model equations of motion describing the ocean circulation.

[64] Results presented here can be summarized as estimates of a time-varying flow field that although still too smooth due to a lack of spatial resolution, simulates many realistic features of the large-scale circulation and includes some that are traditionally missing in numerical coarse-resolution simulations. These latter include vigorous barotropic motion, a more realistic Gulf Stream separation, the correction of the path of the North Atlantic Current, and the presence of an Azores Front in the North Atlantic, among many other features of the global ocean. Käse *et al.* [2001] discuss an application of our estimated surface forcing in a regional high-resolution model of the North Atlantic.

[65] As anticipated, the constrained model has, on average, moved considerably closer to the observations, both those imposed as constraints and those withheld. Also as anticipated, the failure of the model to fully reproduce the observations of either type leads immediately to sometimes difficult issues of determining whether the model is in error or whether the data errors were accurately specified. It is intrinsic to the nature of any statistical estimation procedure that the process of attribution of misfits between model errors and data errors can remain ambiguous and unresolved until further information is obtained. In several cases the comparisons remain indeterminate over large areas of the world ocean because there are too few observations to reduce the data error to levels where it would truly test the model.

[66] The extent to which the present suite of observations would permit a radically different (on a resolved, large

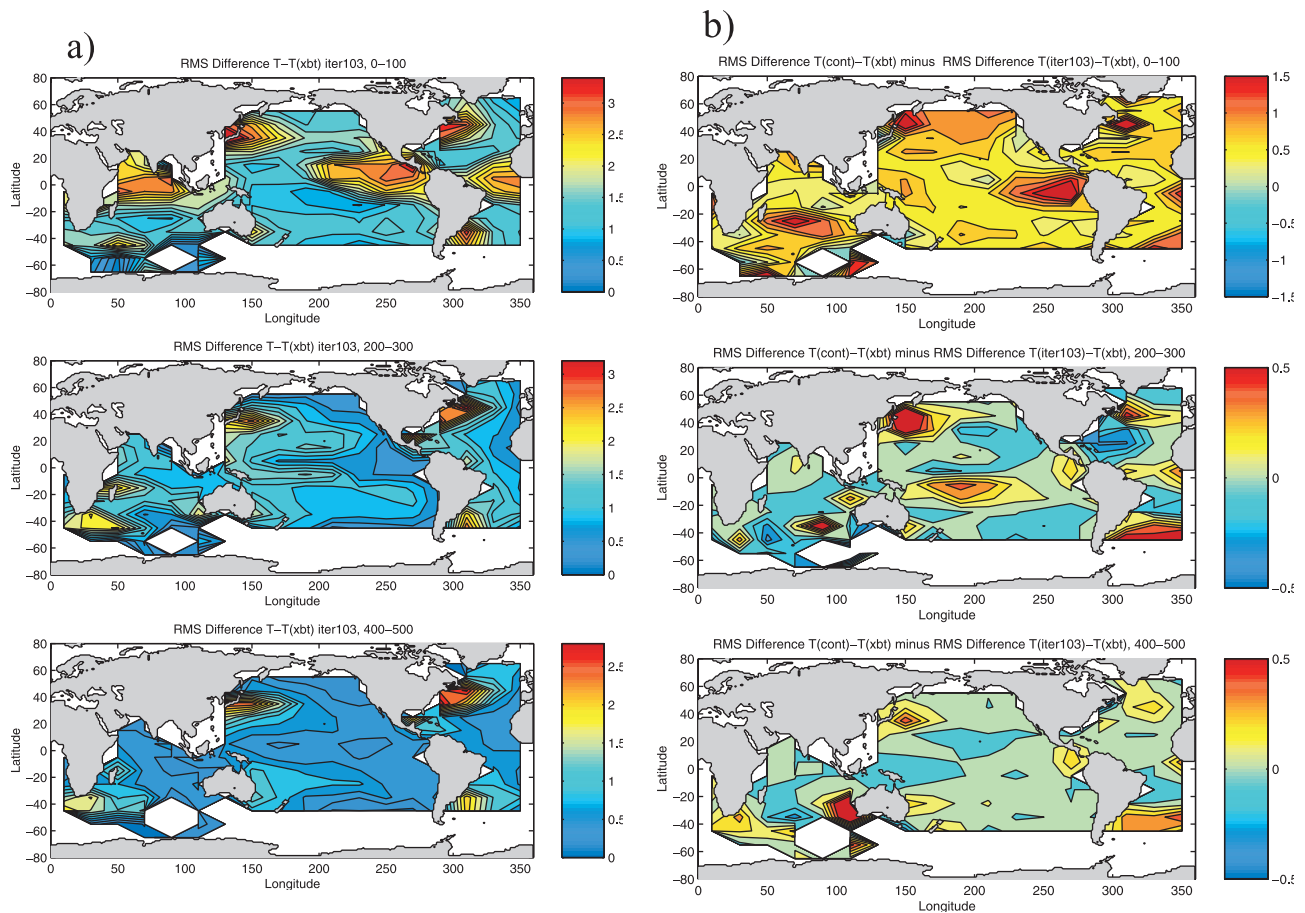


**Figure 20.** (a) RMS differences within  $10^\circ$  regions horizontally and within various 100-m thick depth levels vertically. Shown are resulting fields for, from top to bottom, top 100-, 200- to 300-, and 400- to 500-m depth range. (b) Difference field of RMS misfits shown in Figure 20a minus similar field but based on first guess. Positive values indicate a respective improvement in RMS misfit established through estimation procedure.

scale) general circulation of the ocean remains obscure. It seems unlikely that a truly different solution would be possible (e.g., a large-scale monsoonal shift at great depth in the Indian Ocean) given the geographical breadth both of the climatologies and of the time-continuing observation systems. We have no formal proof of impossibility, and none may be forthcoming. Should, however, the possibility be proven theoretically, it would have very great implications for the design of ocean observing systems.

[67] As the estimates improve through the evolution of numerical models, increasing computer power, and better assimilation schemes, more realistic estimates of the time-evolving flow field will become available that will enable the computation of a host of oceanic processes. However, even with the preliminary results at hand, we can now start to estimate the global heat and freshwater fluxes and divergences as a function of time as demonstrated by Stammer et al. (submitted manuscript, 2002a), calculate the day-by-day variability of the global current system, and diagnose upwelling, potential vorticity fluxes, etc., all in ways that exploit a great variety of data types as well as exploiting the diverse physical processes embodied in the GCM code. There are many other uses of the present results

(e.g., in biological studies), and among the important ones is the possibility of studying the impact and efficiency of various possible oceanic observation systems.

[68] Several immediate improvements in the system can be made. Beyond the incorporation of more data, two steps are particularly important: (1) improved representation of eddy transfers (eddy parameterization) and (2) improved model resolution to 1deg or better. In the long run, we expect to introduce more formal model error estimates, as well as to examine the system sensitivity to the observations by analysis of the adjoint solution [Marotzke et al., 1999]; ultimately, we expect to generate formal error bars for the estimated state.

[69] In summary, we have completed a prototype global ocean state estimate from which we see no fundamental obstacles to moving quickly toward quasioperational estimates and products as envisioned in Global Oceanography Data Assimilation Experiment (GODAE) and other programs. All model fields described here are available through the internet. For details, see the Estimating the Circulation and Climate of the Ocean (ECCO) Project web page (<http://www.ecco-group.org>), where animations of the model results are also provided.

[70] **Acknowledgments.** We thank D. Behringer and Ming Ji at NCEP for providing us with their edited XBT data set. Diana Spiegel and Charmaine King helped with processing of the model fields and WOCE data sets. The help of Lynne Talley and the WOCE SAC (Hamburg) in obtaining preprocessed WOCE hydrographic data is gratefully acknowledged. Valuable comments from two anonymous referees are gratefully acknowledged. Reanalysis surface forcing fields from the National Center for Environmental Prediction/National Center for Atmospheric Research (NCEP/NCAR) are obtained through a computational grant at NCAR. The computational support through a NRAC grant from the National Partnership for Computational Infrastructure (NPACI) is acknowledged. Support was given in part through ONR (NOPP) ECCO grants N00014-99-1-1049 and N00014-99-1-1050, through NASA grant NAG5-7857, through NSF grant OCE 9730071, and through two contracts with the Jet Propulsion Laboratory (958125 and 1205624). This is a contribution of the Consortium for Estimating the Circulation and Climate of the Ocean (ECCO), funded by the National Oceanographic Partnership Program.

## References

- Arakawa, A., and V. R. Lamb, Computational design of the basic dynamical processes of the UCLA General Circulation Model, in *Methods in Computational Physics*, vol. 17, pp. 174–265, Academic, San Diego, Calif., 1977.
- Behringer, D. W., Sea surface height variations in the Atlantic Ocean: A comparison of TOPEX altimeter data with results from an ocean data assimilation system, *J. Geophys. Res.*, *99*, 24,685–24,690, 1994.
- Bennett, A. F., *Inverse Methods in Physical Oceanography*, Cambridge Univ. Press, New York, 1992.
- Chelton, D. B., and A. M. Mestas-Núñez, The large-scale, wind-driven response of the North Pacific, *Int. World Ocean Circ. Exp. Newsl.*, *26*, 3–6, 1996.
- Fukumori, I., R. Raghunath, and L.-L. Fu, Nature of global large-scale sea level variability in relation to atmospheric forcing: A modeling study, *J. Geophys. Res.*, *103*, 5493–5512, 1998.
- Giering, R., and T. Kaminski, Recipes for adjoint code construction, *Trans. Math. Software*, *24*, 437–474, 1998.
- Gilbert, J. C., and C. Lemaréchal, Some numerical experiments with variable-storage quasi-Newton algorithms, *Math. Program.*, *45*, 407–435, 1989.
- Käse, R. H., A. Biastoch, and D. Stammer, On the middepth circulation in the Labrador and Irminger Seas, *Geophys. Res. Lett.*, *28*, 3433–3436, 2001.
- Klinck, J. M., Thermohaline structures of an eddy-resolving North-Atlantic model: The influence of boundary conditions, *J. Phys. Oceanogr.*, *25*, 1174–1195, 1995.
- Koltermann, P., V. Gouretski, and K. Jancke, Hydrographic atlas of the World Ocean Circulation Experiment, vol. 4, Atlantic Ocean, report, World Clim. Res. Prog., World Meteorol. Org., Geneva, in press, 2002.
- Large, W. G., J. C. McWilliams, and S. C. Doney, Oceanic vertical mixing: A review and a model with nonlocal boundary layer parameterization, *Rev. Geophys.*, *32*, 363–403, 1994.
- Lemoine, F., et al., The development of the NASA GSFC and NIMA Joint Geopotential Model, in *International Association of Geodesy Symposia*, vol. 117, *Gravity, Geoid and Marine Geodesy*, edited by J. Segawa et al., pp. 461–469, Springer-Verlag, New York, 1997.
- Levitus, S., R. Burgett, and T. Boyer, *World Ocean Atlas 1994*, vol. 3, *Salinity*, U.S. Dep. of Commer., Washington, D.C., 1994a.
- Levitus, S., R. Burgett, and T. Boyer, *World Ocean Atlas 1994*, vol. 4, *Temperature*, U.S. Dep. of Commer., Washington, D.C., 1994b.
- Malanotte-Rizzoli, P., (Ed.), *Modern Approaches to Data Assimilation in Ocean Modeling*, 455 pp., Elsevier Sci., New York, 1996.
- Marotzke, J., R. Giering, Q. K. Zhang, D. Stammer, C. N. Hill, and T. Lee, Construction of the adjoint MIT ocean general circulation model and application to Atlantic heat transport sensitivity, *J. Geophys. Res.*, *104*, 29,529–29,548, 1999.
- Marshall, J., A. Adcroft, C. Hill, L. Perelman, and C. Heisey, A finite-volume, incompressible Navier-Stokes model for studies of the ocean on parallel computers, *J. Geophys. Res.*, *102*, 5753–5766, 1997a.
- Marshall, J., C. Hill, L. Perelman, and A. Adcroft, Hydrostatic, quasihydrostatic and nonhydrostatic ocean modeling, *J. Geophys. Res.*, *102*, 5733–5752, 1997b.
- Masina, S., N. Pinardi, and A. Navarra, A global ocean temperature and altimeter data assimilation system for studies of climate variability, *Clim. Dyn.*, *17*, 687–700, 2001.
- McPhaden, M. J., et al., The tropical ocean global atmosphere observing system: A decade of progress, *J. Geophys. Res.*, *103*, 14,169–14,240, 1998.
- Milliff, R. F., W. G. Large, J. Morzel, G. Danabasoglu, and T. M. Chin, Ocean general circulation model sensitivity to forcing from scatterometer winds, *J. Geophys. Res.*, *104*, 11,337–11,358, 1999.
- Pavlis, N. K., C. M. Cox, and F. G. Lemoine, Comparison of dynamic ocean topography solutions combining geodetic and oceanographic information (abstract), *Eos Trans AGU*, *80*(17), Spring Meet Suppl., S82, 1999.
- Ponte, R. M., and D. Stammer, The role of regional mass and current changes in the ocean on seasonal polar motions fluctuations, *J. Geophys. Res.*, *104*, 23,393–23,409, 1999.
- Ponte, R. M., D. Stammer, and J. Marshall, Oceanic signals in observed motions of the Earth's pole, *Nature*, *391*, 476–479, 1998.
- Ponte, R., D. Stammer, and C. Wunsch, Improving ocean angular momentum estimates using an ocean model constrained by large-scale data, *Geophys. Res. Lett.*, *28*, 1775–1778, 2001.
- Reynolds, R. W., and T. M. Smith, Improved global sea surface temperature analysis using optimum interpolation, *J. Clim.*, *7*, 929–948, 1994.
- Sirkes, Z., E. Tziperman, and W. C. Thacker, Combining data and a global primitive equation ocean general circulation model using the adjoint method, in *Modern Approaches to Data Assimilation in Ocean Modeling*, edited by P. Malanotte-Rizzoli, pp. 119–145, Elsevier Sci., New York, 1996.
- Spall, M. A., R. A. Weller, and P. W. Furey, Modeling the three-dimensional upper ocean heat budget and subduction rate during the Subduction Experiment J, *Geophys. Res.*, *105*, 26,151–26,166, 2000.
- Stammer, D., Steric and wind-induced changes in TOPEX/Poseidon large-scale sea surface topography observations, *J. Geophys. Res.*, *102*, 20,987–21,010, 1997.
- Stammer, D., C. Wunsch, and R. Ponte, Dealiasing of global high-frequency barotropic motions in altimeter observations, *Geophys. Res. Lett.*, *27*, 1175–1178, 2000.
- Talley, L., Hydrographic atlas of the World Ocean Experiment, vol. 1, Pacific Ocean, report, World Clim. Res. Prog., World Meteorol. Org., Geneva, in press, 2002a.
- Talley, L., Hydrographic atlas of the World Ocean Experiment, vol. 2, Indian Ocean, report, World Clim. Res. Prog., World Meteorol. Org., Geneva, in press, 2002b.
- Woods, J. D., *The Warmwatersphere of the North Atlantic—A Miscellany*, rep. 128, 39 pp., Inst. für Meereskunde, Kiel, Germany, 1984.
- Wunsch, C., *The Ocean Circulation Inverse Problem*, 442 pp., Cambridge Univ. Press, New York, 1996.
- Wunsch, C., and D. Stammer, The global frequency-wavenumber spectrum of oceanic variability estimated from TOPEX/Poseidon altimeter measurements, *J. Geophys. Res.*, *100*, 24,895–24,910, 1995.
- Wunsch, C., and D. Stammer, Satellite altimetry, the marine geoid and the oceanic general circulation, *Ann. Rev. Earth Planet. Sci.*, *26*, 219–254, 1998.

A. Adcroft, C. Eckert, P. Heimbach, C. N. Hill, J. Marshall, and C. Wunsch, Earth and Planetary Science Department, Massachusetts Institute of Technology, 77 Massachusetts Ave., Cambridge, MA 02139-4307, USA. (adcroft@mit.edu; eckert@mit.edu; heimbach@ocean.mit.edu; cnh@ocean.mit.edu; marshall@gulf.mit.edu; cwunsch@pond.mit.edu)

R. Giering, FastOpt, Martinistrasse 21, D-20251 Hamburg, Germany. (Ralf.Giering@fastopt.de)

J. Marotzke, Southampton Oceanography Centre, University of Southampton, European Way, Southampton SO14 3ZH, UK. (jochem.marotzke@soc.soton.ac.uk)

D. Stammer, Scripps Institution of Oceanography, La Jolla, CA 92093, USA. (dstammer@ucsd.edu)